ACS Catalysis

pubs.acs.org/acscatalysis Research Article

Kinetics, Mechanism, and Thermodynamics of Ceria-Zirconia Reduction

Andrew Hwang, Andrew "Bean" Getsoian, and Enrique Iglesia*

Cite This: ACS Catal. 2024, 14, 16184−16204 Read Online

ACCESS | Metrics & More | Article Recommendations | Supporting Information

ABSTRACT: $Ce_{0.5}Zr_{0.5}O_{2-x}$ (CZO) is widely used for the storage and reaction of O atoms (O*) in chemical looping and emissions control. Reductants react with O* to form vacancies (*) at rates limited by surface reactions with O*, replenished through fast diffusion through CZO crystals. The dynamics and mechanism of these surface reactions remain unresolved because O* stability and reactivity depend very strongly on the extent of CZO reduction during stoichiometric reactions. These thermodynamic nonidealities are evident from free energy penalties in removing O* that increase sharply as intracrystalline O* concentrations decrease, leading to reduction rates that deviate from the expected linear dependence of rates on O* concentrations. Rates of CZO reduction by CO, at conditions resembling "cold start" of vehicle emissions systems, decrease 10-fold when O* concentrations decrease by only a factor of 2; this nonlinearity reflects the strong effects of thermodynamic nonidealities on reaction dynamics. This study addresses and resolves these mechanistic and practical matters using transition state theory, a thermodynamic construct that rigorously accounts for the prevalent nonideal behavior. Such formalisms treat $Ce_{0.5}Zr_{0.5}O_2$ as an ideal solution and O*, *, surface-bound intermediates, and transition states as solutes within a well-mixed $Ce_{0.5}Zr_{0.5}O_{2-x}$ solution with excess free energies that depend strongly on extent of reduction. The nonideal behavior of these solutes and the reactivity of O* in reactions with CO are related to the measured thermodynamics of O* through scaling relations, and the requisite kinetic parameters for the ideal system are independently derived from a mechanism-based interpretation of catalytic CO−O_2 reactions on stoichiometric CZO. These approaches and constructs lead to a kinetic model that accurately describes measured transient stoichiometric reduction rates, but only when incorporated into reaction-convection equations that rigorously capture how the thermodynamic activities of kinetically relevant reactants, transition states, and spectators evolve in time and space. These formalisms provide a general framework for the analysis of stoichiometric processes in strongly nonideal systems that are ubiquitous in carbon capture, energy storage, and environmental remediation.

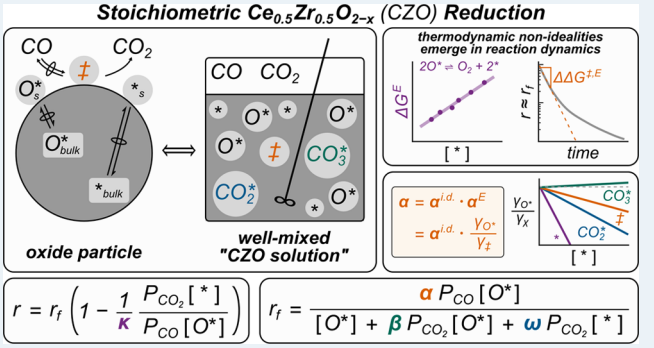

$$r = r_f\left(1 - \frac{1}{\kappa}\frac{P_{CO_2}[*]}{P_{CO}[O^*]}\right) \qquad r_f = \frac{\alpha P_{CO}[O^*]}{[O^*] + \beta P_{CO_2}[O^*] + \omega P_{CO_2}[*]}$$

KEYWORDS: *thermodynamic nonidealities, stoichiometric reactions, solvation effects, kinetic modeling, metal oxides*

1. INTRODUCTION

Stoichiometric fluid−solid reactions are involved in energy storage systems, CO_2 capture technologies, and chemical looping reduction−oxidation processes. These systems invariably embody strong thermodynamic nonidealities as materials change in composition or oxidation state; as a result, the rates of chemical and physical processes cannot be accurately captured using descriptions of (electro)chemical kinetics and mass/ion transport phenomena that neglect such nonideal behavior. Analyses of the dynamics of these processes can then lead to incomplete mechanistic interpretations and to their attribution to incorrect physicochemical causes. For instance, open circuit potentials of lithium-based electrodes depend sensitively on the extent of lithiation, which Tafel equations do not explicitly include, thus precluding physics-based models of (dis)charge and degradation rates in Li-ion batteries.[1,2] This study develops protocols that address these complexities through analogies to solution-phase equilibria in nonideal mixtures using formalisms and concepts that are emerging in treating the effects of solvents on reaction rates.

Chemical and physical processes occur at rates that reflect the tendency of the system to approach thermodynamic equilibrium. The dynamics of these processes are driven by gradients in chemical potential, whether processes involve a phase change, mass transport, or (electro)chemical reactions. Solvents affect reaction rates by (de)stabilizing the reactants, intermediates, and/or transition states present along chemical

Received: August 9, 2024
Revised: October 4, 2024
Accepted: October 4, 2024
Published: October 18, 2024

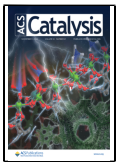

or physical trajectories. Transition state theory provides the formalism necessary to understand, model, and predict these solvation effects whether in ideal or nonideal systems in their thermodynamic contexts.

Transition state theory posits a quasi-equilibrium between a transition state (TS) and reactants of an elementary step and crossing rates that are proportional to the concentration of transition states.[3−6] Solvents can affect reaction rates only when they (de)stabilize to different extents the TS and reactants in a kinetically relevant elementary step along a reaction coordinate. This formalism has been successfully used to account for solvation effects observed for rates of homogeneous reactions in solution[7−9] and reactions on surfaces,[10−12] with effects, in most cases, imposed by changes in the identity of the solvent. For instance, chemical reaction rates at active sites confined within voids of molecular dimensions are significantly altered by changing the size and shape of such voids, because they "solvate" reactants, intermediates, and transition states through van der Waals forces, often to different extents,[12−15] or by intrapore liquids that (de)stabilize guest molecules through noncovalent or electrostatic interactions.[16−18] Here, this formalism is transferred to stoichiometric fluid−solid reaction systems that exhibit very strong thermodynamic nonidealities as a consequence of temporal (and spatial) changes in the extent of reduction or oxidation during stoichiometric cycling. In these systems, "solvation effects" on rate emerge and evolve innately as the reaction proceeds, instead of doing so in response to a change in the solvating properties of an external environment, such as a different solvent or a confining void of different size.

Ceria-zirconia solid solutions ($Ce_{0.5}Zr_{0.5}O_{2-x}$, $x \in [0, 0.25]$; CZO) are used as oxygen carriers for chemical looping redox cycles[19] and as electrolytes in solid oxide fuel cells;[20] they are also used as oxygen storage devices in emissions control systems.[21−23] These applications exploit the durable redox properties and the fast diffusion of lattice O-anions of Ce-based oxides.[19−24] Lattice oxygen anions react with reductants, such as CO and hydrocarbons, at crystallite surfaces during a reduction half-cycle, and the anion vacancies formed are filled by oxidants (usually O_2), thereby completing a reduction−oxidation cycle. The Gibbs free energy for the removal of an O atom from $Ce_{0.5}Zr_{0.5}O_{2-x}$ (ΔG_{red}) becomes increasingly unfavorable (more positive) with increasing extent of CZO reduction ($\xi_{red} = 4x$);[24−26] archived thermodynamic data show that a change in extent of reduction ($\Delta\xi_{red}$) of 0.2 leads to a change in free energy ($\Delta\Delta G_{red}$) of more than 60 kJ mol^{-1} at 873 K.[26] Such strongly nonideal redox thermodynamics impart intrinsic nonuniformities to the dynamics of O atom removal and addition reactions. As CZO crystals become depleted/enriched of O atoms, the intrinsic rate of O atom removal/addition decreases much more sensitively than expected from the remaining number of O atoms, indicative of their lower reactivity. These nonidealities preclude conventional kinetic and transport analyses of reaction and diffusion mechanisms and their usefulness in interpreting the effects of crystal phase, phase purity, and size on rates of reduction and oxidation half-cycles.

This study addresses these hurdles by treating lattice oxygen anions (O*) and anion vacancies (*) as solutes within "well-mixed" $Ce_{0.5}Zr_{0.5}O_{2-x}$ crystals. This analogy to fluid-phase equilibria for interpreting kinetic data and the ability to extract from them mechanistic insights about surface reactions require that the "solution" be well-mixed. Intracrystalline gradients in the chemical potential of oxygen anions (and thus of anion vacancies) are absent during reduction of CZO by CO, such that O atom removal rates solely reflect the rate of surface reactions at conditions relevant to the use of CZO as an oxygen buffer in three-way catalysts.[27] Measurements of redox thermodynamics inform about how the solubilities of O* and * change with ξ_{red} and how it does so among samples with differing Ce/Zr ratios and crystal structure and size. The thermodynamic underpinnings of transition state theory then provide the requisite framework to relate the (excess) free energy differences between oxygen anions and anion vacancies to those for the other "solutes" that emerge along reaction trajectories in CZO redox half-cycles—namely, transition states and surface-bound intermediates. Thus, the consequences of intrinsic nonuniformities in redox thermodynamics on surface reaction dynamics can be understood, modeled, and predicted using the same formalisms previously used to describe solvation effects for thermodynamically nonideal systems in surface catalysis.[7−18]

These formalisms are illustrated here by showing that stoichiometric rates of CZO reduction by CO, measured at relevant conditions of practice, are limited by the CO-mediated oxygen anion removal elementary step, which forms vacancy-bound carboxylates (CO + O* → CO_2*). The solubility (and stability) of the kinetically relevant transition state decreases and that of rate-inhibiting carboxylates increases as $Ce_{0.5}Zr_{0.5}O_{2-x}$ solutions become depleted of O-anions. Thus, CZO reduction reactions ultimately reach nearly undetectable rates before equilibrium can be achieved in practical times, because the desorption of carboxylates and the depletion of residual O atoms become more unfavorable as reduction occurs. These mechanistic insights for these stoichiometric reactions were recognized only after developing an accurate rate equation, a development aided by assessing the kinetics and mechanism of catalytic CO oxidation and the decomposition of carbonates and carboxylates on CO_2-treated CZO crystals, and then embedding the rate equation into reaction-convection models that rigorously account for the temporal and spatial gradients within a CZO packed bed. Axial gradients cannot be neglected even when the relative changes in CO and CO_2 concentration are negligibly small, because exceedingly small gradients in ξ_{red} have profound consequences on the solubilities of O atom removal transition states and CO_2-derived adsorbates, as inferred from redox thermodynamic measurements and free energy and scaling relationships.

The protocol described and used in this study accurately captures kinetic data of transient stoichiometric processes affected by strong effects of the extent of reduction (and the O-content) on the stability and reactivity of reactants and products by implementing concepts from the canon of surface kinetics within the conceptual framework of (nonequilibrium) thermodynamics and transition state theory. This approach is agnostic about the types of fluids, solids, and energy-stimuli (e.g., heat, photons, and electricity) in the system of interest. The methods and formalisms illustrated here for reduction−oxidation of metal oxides can be leveraged to deduce mechanistic insights and to identify materials and process design criteria for other systems in which thermodynamic nonidealities have prevailed to hinder the use of rigorous kinetic analyses in such inquests. Examples of such systems that also have extensive archives of essential thermodynamic data include carbonation-calcination of metal (hydr)oxides,

https://doi.org/10.1021/acscatal.4c04771
ACS Catal. 2024, 14, 16184−16204

CO_2 uptake-release on amine-based sorbents, electrochemical separations for metals recovery, (de)intercalation of layered cathode materials, and selective oxidations via chemical looping.

2. MATERIALS AND METHODS

The provenance and characterization of the CZO samples and the treatment protocols used were previously reported.[27] Briefly, CZO nanocrystals (Ford Motor Company) were treated by sequential reduction (1% H_2, 3% CO in N_2) and oxidation (4% O_2 in N_2) cycles at 1133 K (240 cycles over 16 h), intended to anneal the samples into thermodynamically stable form and to mimic prolonged exposure to rich-lean combustion cycles in vehicle emission systems. The results of the structural and compositional characterization tests for the parent (120 m^2 g^{-1}, 4.8 nm crystals) and redox-aged (40 m^2 g^{-1}, 9.6 nm) samples were consistent with those expected for the fluorite $Ce_{0.5}Zr_{0.5}O_2$ phase (Ce/Zr = 0.94). Experiments to evaluate the thermodynamics and kinetics of CZO reduction and oxidation were conducted on the redox-aged sample to ensure that measurements reflect properties intrinsic to $Ce_{0.5}Zr_{0.5}O_{2-x}$ instead of extrinsic nonuniformities (e.g., structural defects) or of reaction-induced changes in properties or crystal morphology.

Stoichiometric CZO reduction and oxidation reactions by CO and CO_2, respectively, were conducted using the same reagents, apparatus, and treatment protocols described in an earlier report.[27] These transient reactions were performed in a packed-bed quartz reactor (0.4 cm i.d.) with plug-flow hydrodynamics; the composition of reactant and product streams was continuously assessed using online infrared (MKS MultiGas) and mass spectrometric (Leybold Inficon) methods. The reactor was held within a resistively heated crucible furnace (National Element), and its temperature was controlled and monitored using an electronic controller (Watlow) and K-type thermocouple affixed to the outer reactor wall near the axial packed-bed center. The packed beds consisted of mixtures of CZO aggregates (180−250 μm) and inert quartz granules (180−250 μm) in >10:1 (w/w) quartz/CZO mass ratios. Before reduction reactions, samples were treated at 1000 K for 1 h in flowing 20 kPa O_2 in He, cooled to the target reaction temperature (648 or 873 K), and then flushed with a pure He stream. This oxidative treatment sought to desorb adventitious impurities (atmospheric CO_2 and H_2O) and to ensure that samples were fully oxidized ($Ce_{0.5}Zr_{0.5}O_2$; $\xi_{red,0} = 0$) before exposure to reactant mixtures (0.20−4.1 kPa CO, 0.18−81 CO/CO_2). Oxidation reactions were conducted on partially reduced $Ce_{0.5}Zr_{0.5}O_{1.83}$ samples, which were obtained by treating the fully oxidized ones in flowing H_2 (5.0 kPa) at 1000 K for 2 h; the extent of reduction ($\xi_{red,0} \approx 0.7$) was determined by monitoring the amounts of H_2 consumed and H_2O formed, which agreed within experimental error. The partially reduced samples were flushed in flowing He at 1000 K for 1 h and then cooled to the target reaction temperature before exposure to CO_2−CO mixtures.

Catalytic rates of aerobic CO oxidation on $Ce_{0.5}Zr_{0.5}O_2$ were measured at 648 K in excess O_2 ($O_2/CO \geq 1$) using the same reactor and analytical protocols and oxidative thermal treatment described above for stoichiometric reactions. Rates remained unchanged during 10 h time. Weisz-Prater and Mears criteria[28] were used to confirm that measured rates were not corrupted by intra- and interphase transport artifacts (Section S1; Supporting Information; SI). CO_2 formation rates measured using packed beds with 10:1 and 25:1 (w/w) quartz/CZO dilution ratios were the same, confirming the absence of kinetically consequential axial or radial temperature gradients. This result for the catalytic reactions serves also to confirm the isothermal nature of stoichiometric reduction experiments, for which the rates of heat release were significantly smaller than those in catalytic experiments.

The stability and reactivity of CO_2-derived bound species on oxidized ($\xi_{red,0} = 0$) and partially reduced ($\xi_{red,0} \approx 0.4$ or 0.7) $Ce_{0.5}Zr_{0.5}O_{2-x}$ crystals were assessed by measuring the evolution of CO_2 and CO during temperature ramping using the same apparatus as for stoichiometric and catalytic reactions. The reductive thermal treatment used to obtain the $Ce_{0.5}Zr_{0.5}O_{1.90}$ sample ($\xi_{red,0} \approx 0.4$) was also the same as that described above for the $Ce_{0.5}Zr_{0.5}O_{1.83}$ sample ($\xi_{red,0} \approx 0.7$) but at lower temperature (700 K instead of 1000 K) for 2 h in flowing 5.0 kPa H_2 in He. A CO_2 stream (2.0 kPa in He) was passed over the CZO sample (400 molec. CO_2 (nm CZO)$^{-2}$ h^{-1}) at 340 K for 0.5 h to adsorb CO_2. The reactor was then flushed with flowing He (8.3 cm^3 g^{-1} s^{-1}) at 340 K for 0.5 h to ensure complete removal of weakly bound species; CO_2 concentrations in reactor effluent mixtures reached undetectable levels after <0.1 h of inert purging. The samples were then heated to 1000 K (0.33 K s^{-1}) in flowing He. CO_2 and CO were the only species detected in product streams, with the latter being formed only when CZO was partially reduced, indicative of vacancies being repopulated by O atoms within CO_2 adsorbates.

3. RESULTS AND DISCUSSION

3.1. Reduction−Oxidation Equilibria of Ceria-Zirconia Solid Solutions: An Analogy to Solution Thermodynamics.

Thermodynamic data for reduction−oxidation equilibria of metal oxides are typically reported from measurements of O_2 evolution reactions:[24−26,29−32]

$$\frac{2}{x}Ce_{0.5}Zr_{0.5}O_2 \rightleftharpoons \frac{2}{x}Ce_{0.5}Zr_{0.5}O_{2-x} + O_2 \quad (1)$$

Equilibrium values of x at given O_2 pressures are determined from the numbers of O atoms removed/added in gas−solid reduction/oxidation reactions with reactant streams containing reductant-oxidant pairs (e.g., CO−CO_2 or H_2−H_2O) at various reductant to oxidant ratios and then calculating the corresponding virtual O_2 pressures[33] using gas-phase thermodynamics for CO or H_2 combustion.

Figure 1 shows the ratio of the average CO_2 pressure along the bed (using inlet and outlet values; $\langle CO_2 \rangle$) to the average CO pressure ($\langle CO \rangle$) versus extent of reduction (ξ_{red}) during $Ce_{0.5}Zr_{0.5}O_2$ reduction (solid, $\xi_{red,0} = 0$) and $Ce_{0.5}Zr_{0.5}O_{1.82}$ oxidation (dashed, $\xi_{red,0} = 0.71$) performed at 873 K with a reactant stream comprising 1.0 kPa CO and 1.0 kPa CO_2, which corresponds to a virtual O_2 pressure of 1.9×10^{-21} bar.[34] The abscissa values were calculated at each point in time ($\xi_{red}(t)$) by integrating measured rates up to that time (t):

$$\xi_{red}(t) = \xi_{red,0} + \int_0^t r_{CO_2}(t')dt' = \xi_{red,0} - \int_0^t r_{CO}(t')dt' \quad (2)$$

In eq 2, r_{CO_2} and r_{CO} are the net rates of CO_2 and CO formation (normalized by the number of removable O atoms

https://doi.org/10.1021/acscatal.4c04771
ACS Catal. 2024, 14, 16184−16204

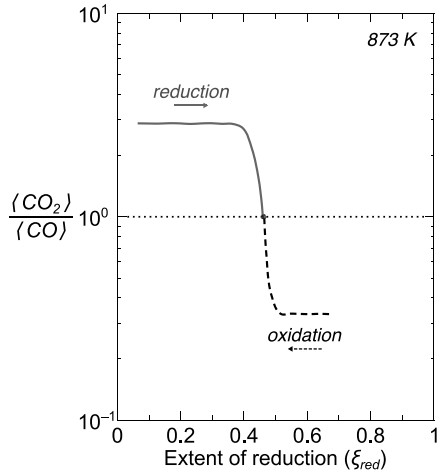

Figure 1. Ratio of average CO_2 and CO pressures ($\langle CO_2\rangle/\langle CO\rangle$) versus extent of reduction (ξ_{red}) for $Ce_{0.5}Zr_{0.5}O_2$ reduction (solid) and $Ce_{0.5}Zr_{0.5}O_{1.82}$ oxidation (dashed) reactions conducted at 873 K and using reactant streams with 1.0 kPa CO and 1.0 kPa CO_2.

in stoichiometric CZO; $1.69{\cdot}10^{-3}$ mol_O g^{-1}). CO_2 forms and CO is consumed in the reduction reaction (solid trace) leading to $\langle CO_2\rangle/\langle CO\rangle$ values that exceed the CO_2/CO ratio in the inlet stream (1.0). Net CO_2 formation rates ultimately reach undetectable levels and reduction ceases upon reaching a final ξ_{red} of 0.46. This value is the same as that obtained in the oxidation reaction (dashed trace; 0.46). Such similar ξ_{red} values show that (at 873 K and 1.9×10^{-21} bar virtual O_2 pressures) redox equilibria is achieved and that the equilibrium ξ_{red} value is 0.46. The final ξ_{red} values from both directions (reduction and oxidation) were also the same at all tested virtual O_2 pressures (2.3×10^{-19} to 1.1×10^{-24} bar), giving equilibrium ξ_{red} values between 0.41 to 0.54.

These thermodynamic data can also be expressed as Gibbs free energies for the reduction−oxidation reaction (eq 1) using a convention[35] that sets the thermodynamic activity of all pure solids ($Ce_{0.5}Zr_{0.5}O_2$ and $Ce_{0.5}Zr_{0.5}O_{2-x}$, here) to unity.[24−26,29−32] A different (and equally arbitrary) convention is defined and adopted here to enable the use of nonideal and nonequilibrium thermodynamic formalisms in examining reduction−oxidation reaction dynamics. This convention considers oxygen anions (O*) and anion vacancies (*) as solutes within a "well-mixed" $Ce_{0.5}Zr_{0.5}O_{2-x}$ crystal and depicts O_2 evolution as occurring upon the removal of two O* from the solution, which by charge neutrality requires the dissolution of two *:

$$2O^* \rightleftharpoons 2^* + O_2 \tag{3}$$

The well-mixed assumption for this "CZO solution" (required for this treatment) was confirmed by three different types of experiments each showing that lattice diffusion is much faster than the surface reaction with CO during CZO reduction.[27] One type compared O atom removal rates with different reductant-oxidant pairs but at the same gas-phase redox potential and thus equivalent driving forces for lattice diffusion. Reduction rates measured using CO−CO_2 and H_2−H_2O mixtures were different, which implies that lattice diffusion is not the rate-limiting process. Another experiment compared the rates of reduction by CO for CZO crystals with and without Pt nanoparticles dispersed on their surfaces, such particles could influence rates of surface reactions, but not bulk lattice diffusion rates. The prevalent atomic contact between Pt nanoparticles and CZO crystal surfaces led to higher O atom removal rates, a demonstration of the kinetic relevance of surface reactions. A third type of experiment imposed inert "dwell" periods at various stages along stoichiometric O atom removal processes by CO; any intracrystalline gradients in O* chemical potential would disappear during these dwells, leading to an increase in reduction rate upon resuming the reaction. These increases were not detected, indicating that "CZO solutions" are well-mixed during these stoichiometric reduction reactions. These independent measurements provide compelling evidence that O* and * chemical potentials are uniform throughout CZO crystals, the requisite criteria for a well-mixed solution.

The equilibrium criterion for eq 3 gives (details in Section S2; SI):

$$\exp\left(-\frac{\Delta G_{red}^{\ominus}}{RT}\right) = \left(\frac{a_*}{a_{O^*}}\right)^2\left(\frac{P_{O_2}}{P^{\ominus}}\right) \tag{4}$$

where P_{O_2} is the O_2 pressure, a_{O^*} and a_* are the activities of O* and * solutes, and $P^{\ominus}$ and $\Delta G_{red}^{\ominus}$ are the total pressure and Gibbs free energy change at an arbitrary condition chosen here as an ideal gas at standard conditions (273.15 K, 1 bar) for O_2 and a $Ce_{0.5}Zr_{0.5}O_{2-x}$ crystal at infinite dilution in anion vacancies (*; $\xi_{red} \to 0$) for the solution-phase. The ratio of O* and * activities at the reference condition ($\xi_{red} \to 0$) is defined to be unity, such that $\Delta G_{red}^{\ominus}$ values represent the Gibbs free energy change of eq 3 for CZO crystals with ξ_{red} values that asymptotically approach zero, the "ideal solution".[36] The activities of each solute are given by the product of its activity coefficient and concentration ($a_j = \gamma_j{\cdot}[j]$, j = O* or *), and the concentrations are related to ξ_{red} via charge balance. Equation 4 then becomes

$$\exp\left(-\frac{\Delta G_{red}^{\ominus}}{RT}\right)\left(\frac{\gamma_{O^*}}{\gamma_*}\right)^2 = \left(\frac{\xi_{red}}{1-\xi_{red}}\right)^2\left(\frac{P_{O_2}}{P^{\ominus}}\right) \tag{5}$$

Ratios of O* and * activity coefficients (γ_{O^*}/γ_*) become smaller as O* solubility increases relative to that for * in the CZO solvent. The definition of partial molar excess Gibbs free energies ($\bar{G}_j^E = RT\ln\gamma_j$)[37] can be inserted into eq 5 to give:

$$\exp\left(-\frac{\Delta G_{red}}{RT}\right) \equiv \exp\left(-\frac{\Delta G_{red}^{\ominus} + \Delta G_{red}^{E}}{RT}\right) = \left(\frac{\xi_{red}}{1-\xi_{red}}\right)^2\left(\frac{P_{O_2}}{P^{\ominus}}\right) \tag{6}$$

The Gibbs free energy change for O_2 evolution (ΔG_{red}) is the sum of the ideal solution and the excess Gibbs free energy changes ($\Delta G_{red}^{\ominus} + \Delta G_{red}^{E}$). The former ($\Delta G_{red}^{\ominus}$) depends only on temperature and pressure, because the chemical potential of O*, *, and O_2 at the reference condition depend only on temperature and pressure, while excess values ($\Delta G_{red}^{E} = 2RT\ln(\gamma_*/\gamma_{O^*})$) are influenced by interactions with the CZO solvent. Thermodynamic nonidealities are represented by nonzero excess Gibbs free energy changes, which become more positive as O-anions become more stable relative to anion vacancies and as O_2 evolution (eq 3; and CZO reduction; eq 1) becomes increasingly unfavorable as a result.

Thermodynamic data for CZO reduction−oxidation, given by equilibrium ξ_{red} values at each virtual P_{O_2} (Figure 1), are

https://doi.org/10.1021/acscatal.4c04771
ACS Catal. 2024, 14, 16184−16204

interpreted here in the context of ΔG_{red} values (eq 6). These metrics of thermodynamic nonidealities are calculated based on the chosen convention defined above ($a_*/a_{O^*} \rightarrow 1$ as $\xi_{red} \rightarrow 0$), which is convenient and as equally arbitrary as setting activities of unity for pure solids;[35] such an approach uses the formalisms and lexicon of thermodynamic treatments for describing the effects of nonidealities on chemical dynamics by nonequilibrium thermodynamics (Section 3.2). Figure 2 shows

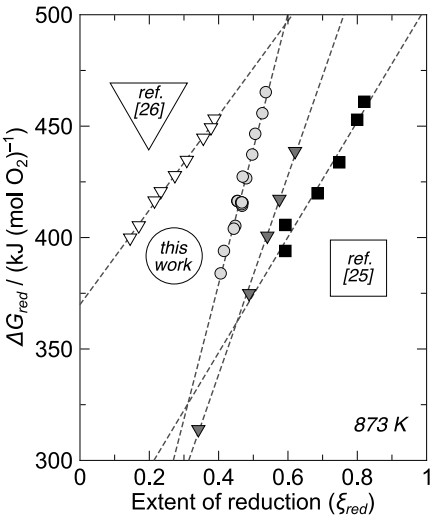

Figure 2. Thermodynamic data for reduction−oxidation of $Ce_{0.5}Zr_{0.5}O_{2-x}$ at 873 K in terms of the Gibbs free energy change for the O_2 evolution reaction (ΔG_{red}; eqs 3 and 6) versus extent of reduction (ξ_{red}). The black squares represent data from ref 25 and the open and dark-gray triangles from ref 26; the light-gray circles denote data collected in this study. The dashed lines represent those of best-fit determined via linear regression to ΔG_{red} versus ξ_{red} data sets to the functional form of eq 7.

values of ΔG_{red} at different ξ_{red} values from CZO reduction−oxidation thermodynamic data reported here (light-gray circles) and reported previously (black squares,[25] and open and dark-gray triangles[26]).

These data were collected on different $Ce_{0.5}Zr_{0.5}O_{2-x}$ samples and discrepancies among them may merely reflect their different crystal size and/or phase purity. Nevertheless, all samples show similar trends; the ΔG_{red} values increase linearly as ξ_{red} increases. This trend indicates that CZO reduction becomes less favorable as ξ_{red} increases; in other words, the CZO solvent preferentially stabilizes O* over * solutes as it becomes depleted of O* (and enriched in *). These changes in the nature of the solvent are very strong. For the sample used in the present study (light-gray circles), a $\Delta\xi_{red}$ change of 0.2 leads to a $\Delta\Delta G_{red}$ change of about 100 kJ mol^{-1}. Such changes are very large in comparison with the solubility of NaCl in water and DMF, for which the ratio of solubility constants (K_{sp}) correspond to free energies of dissolution that differ by less than 20 kJ mol^{-1}.[38]

The dashed lines in Figure 2 were derived from linear regressions of these thermodynamic data to the functional form:

$$\frac{\Delta G_{red}}{RT} = \frac{\Delta G^{\ominus}_{red}}{RT} + \frac{\Delta G^{E}_{red}}{RT} = \frac{\Delta G^{\ominus}_{red}}{RT} + (m_{red}\cdot\xi_{red}) \quad (7)$$

For each data set, the linear relationship between ΔG_{red} and ξ_{red} shows that the solvation effects, for a given CZO sample at a given temperature, are well-described by a single-valued function of ξ_{red}, given by the functional form in eq 7. This linear relation resembles the phenomenological relations used to describe activity coefficients and excess Gibbs free energies for highly concentrated electrolyte solutions.[39,40] Scaling relations between excess Gibbs free energies for O_2 evolution (ΔG^{E}_{red}; eq 7) and those for the formation of kinetically relevant transition states imply that the latter can also be described as single-valued functions of ξ_{red} (*vide infra*).

The discrepancy in the absolute ΔG_{red} values, but not in their trends with ξ_{red}, among these four data sets in Figure 2, cannot be attributed to differences in bulk Ce/Zr composition (all samples consist of $Ce_{0.5}Zr_{0.5}O_{2-x}$ crystals). They are likely to reflect instead differences in nanocrystal size, crystal structure, phase purity, cation (dis)ordering, and/or extent of annealing and its consequences for the density of defects or crystal imperfections. The data shown as open triangles (ref 26), light-gray circles (this work), and black squares (ref 25) were collected on CZO samples with mean nanocrystal diameters of 8, 9.6, and 17 nm, respectively. The CZO crystal size for the sample shown as dark-gray triangles (ref 26) was not reported, but it is presumably larger than 8 nm, because it was prepared by "aging" 8 nm crystals (open triangles) via reduction−oxidation cycling.[26] The equilibrium ξ_{red} values at a given virtual O_2 pressure increase with increasing crystal size, indicating that larger crystals are more reducible in this thermodynamic context; for instance, at 1.0×10^{-23} bar O_2, ξ_{red} values increase from 0.29, 0.47, to 0.64 as crystal size increases from 8 to 17 nm. Similar systematic trends between nanoparticle size and redox thermodynamics have been reported for Co- and Fe-oxides.[41,42]

These consequences of nanoparticle diameter on redox thermodynamics reflect, in part, the larger free energy penalties incurred in removing surface instead of bulk O atoms. Moreover, for semiconducting oxides, such as CZO, such size effects also reflect quantum confinement effects that underpin the size-dependent band gaps of quantum dots.[43,44] The smaller slopes in the ΔG_{red} trends with ξ_{red} (m_{red} in eq 7) in as-prepared samples (open triangles and black squares, Figure 2) compared with those for the redox-aged samples (light-gray circles and dark-gray triangles) are likely to reflect extrinsic nonuniformities that are annealed by repeated reduction−oxidation cycling, thus rendering the resulting CZO crystals more uniform (and thermodynamically stable) than as-prepared samples. These cycles are also likely to narrow crystal size distributions and to minimize crystal-to-crystal variations in Ce and Zr location within CZO lattices. Thus, the thermodynamic and kinetic data collected on redox-aged samples are likely to reflect intrinsic nonuniformities with minimal contributions from heterogeneities in structural properties resulting from specific synthesis protocols.

This analysis of reduction−oxidation data shows that the inherent thermodynamic nonidealities of solutions of oxygen anions and anionic vacancies in $Ce_{0.5}Zr_{0.5}O_{2-x}$ solvents can be described accurately, for a given CZO sample, by ξ_{red}. These

https://doi.org/10.1021/acscatal.4c04771
ACS Catal. 2024, 14, 16184−16204

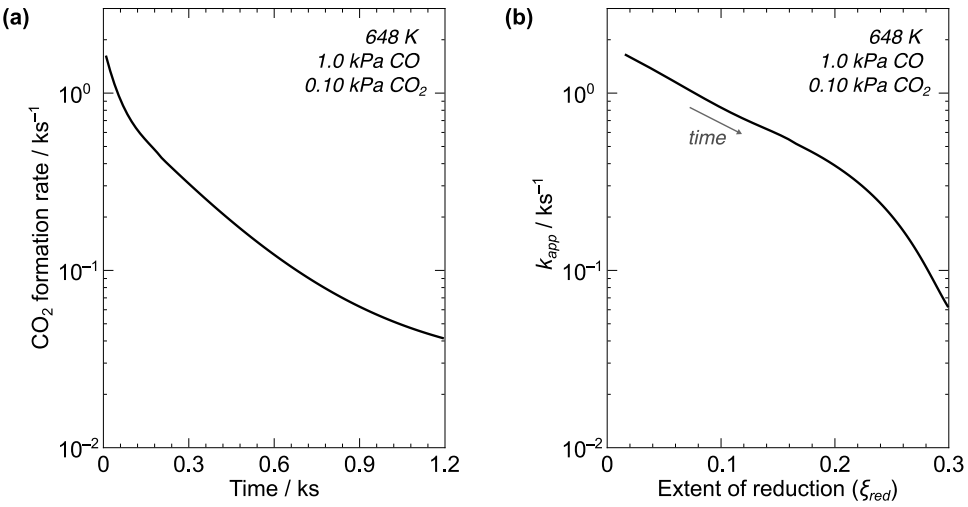

Figure 3. (a) CO_2 formation rate normalized by the total amount of removable O atoms versus time and (b) apparent first-order rate parameters (k_{app}, eq 8) versus extent of reduction (ξ_{red}) for $Ce_{0.5}Zr_{0.5}O_2$ reduction at 648 K, 1.0 kPa CO, and 0.10 kPa CO_2.

nonidealities also strongly influence the dynamics of CZO reduction and oxidation processes, for which the tenets of transition state theory provide the requisite framework to relate redox thermodynamics to chemical reaction rates.

3.2. Kinetic Trends and Consequences of Thermodynamic Non-Idealities for Stoichiometric CZO Reduction Rates. Rates of fluid−solid reactions depend on the activities of species bound at surfaces, which are strictly proportional to adsorbate concentrations only for thermodynamically ideal (and infinitely dilute) systems. Rates of stoichiometric CZO reduction are expected to depend nonlinearly on the concentration of oxygen anion reactants (O*), because the thermodynamics of $Ce_{0.5}Zr_{0.5}O_{2-x}$ reduction−oxidation processes exhibit marked nonidealities (Section 3.1). The same solvation effects that cause the strong ξ_{red} effects on O* and * solubilities (Figure 2) also affect the activity coefficients (and the excess free energy barriers) for species involved in kinetically relevant steps in CZO reduction reactions. These consequences of thermodynamic nonidealities on reaction dynamics become apparent when examining profiles of O atom removal rates versus time, as shown in Figure 3.

Figure 3a shows CO_2 formation rates (per removable O atoms in CZO) as time evolves during reactions of CO (1.0 kPa) with stoichiometric $Ce_{0.5}Zr_{0.5}O_2$ samples ($\xi_{red,0} = 0$) at 648 K; CO_2 (0.10 kPa) was added to the inlet stream in order to dampen axial bed gradients in CO_2/CO ratios. O atom removal rates decreased monotonically with time, but with trends that do not conform to the simple exponential form expected for first-order kinetics in O* for thermodynamically ideal systems, for which the slopes of the semilogarithmic plots in Figure 3a would remain constant with time and ξ_{red}. These data show that the slopes, which reflect an apparent first-order rate parameter for O* removal, become smaller as O* is depleted with time; this reflects the thermodynamic nonidealities of the reduction dynamics and the greater stability (and lower reactivity) of O* as ξ_{red} increases. These apparent first-order rate parameters (k_{app}),

$$k_{app}(t) = \frac{r_{CO_2}(t)}{[O^*](t)} = \frac{r_{CO_2}(t)}{1 - \xi_{red}(t)} \tag{8}$$

are defined as the ratio between CO_2 formation rate ($r_{CO_2}(t)$) and the concentration of residual removable O atoms ($[O^*](t)$) at each time t, where the values of $[O^*](t)$ are related to $\xi_{red}(t)$ via charge balance (eq 2). Figure 3b shows k_{app} values that decrease monotonically as ξ_{red} increases (thirty-fold as ξ_{red} increases from 0 to 0.3); in thermodynamically ideal systems, k_{app} would be insensitive to ξ_{red}. These trends show that the free energy barriers that must be overcome for CO to remove an O atom from $Ce_{0.5}Zr_{0.5}O_{2-x}$ increase sharply as ξ_{red} increases and as O* solutes become more stable in a "CZO solution" that becomes increasingly dilute in O*. Transition state theory provides the formalism necessary to interpret these consequences of thermodynamic nonidealities on surface reaction dynamics using the same analogy to solution-phase equilibria used in the preceding section to describe reduction−oxidation equilibria.

Transition state theory posits the existence of a transition state (TS) between the reactant and product states of an elementary step. The activity of this TS (a_{TS}) is described by its (quasi)equilibrium with reactants, and the rate is assumed to be strictly proportional to the concentration of transition states ($[TS] = a_{TS}/\gamma_{TS}$).[7−18] These tenets lead to an equation for the rate of an elementary step between CO and an oxygen anion:

$$\begin{aligned} r &= \frac{k_B T}{h}\exp\left(-\frac{\Delta G_{app}^{\ominus,\ddagger}}{RT}\right)\frac{P_{CO}a_{O^*}}{\gamma_{TS}} \\ &= \left[\frac{k_B T}{h}\exp\left(-\frac{\Delta G_{app}^{\ominus,\ddagger}}{RT}\right)\frac{\gamma_{O^*}}{\gamma_{TS}}P_{CO}\right][O^*] \\ &= \left[\frac{k_B T}{h}\exp\left(-\frac{\Delta G_{app}^{\ominus,\ddagger} + \Delta G_{app}^{E,\ddagger}}{RT}\right)P_{CO}\right][O^*] \end{aligned} \tag{9}$$

where $\Delta G_{app}^{\ominus,\ddagger}$ is the Gibbs free energy of formation of the TS from CO and O* reactants for the ideal-solution reference condition ($\xi_{red} \to 0$) and $\Delta G_{app}^{E,\ddagger}$ is the respective excess Gibbs free energy of formation; the latter term captures how the thermodynamically nonideal $Ce_{0.5}Zr_{0.5}O_{2-x}$ solvent (de)-stabilizes the reactant (O*) and transition state (TS) solutes.

https://doi.org/10.1021/acscatal.4c04771
ACS Catal. 2024, 14, 16184−16204

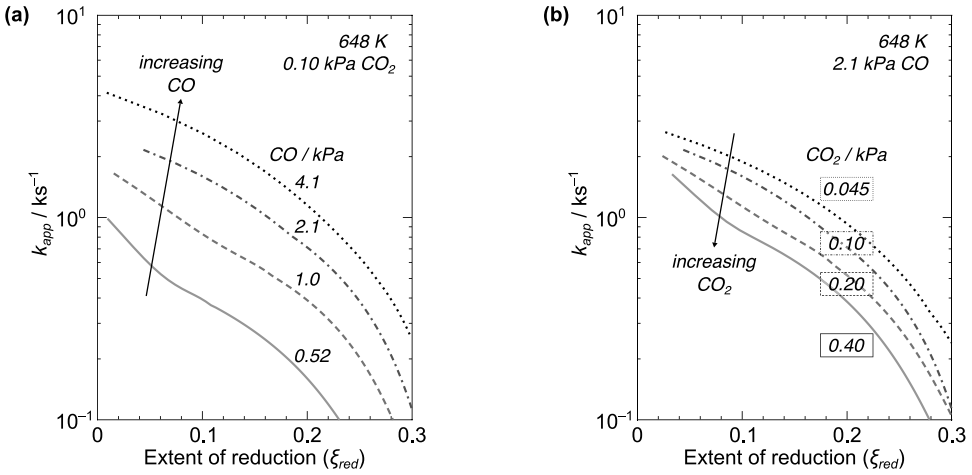

Figure 4. Apparent first-order rate parameters (k_{app}, eq 8) versus extent of reduction (ξ_{red}) for $Ce_{0.5}Zr_{0.5}O_2$ reduction at 648 K. (a) Reactions performed with the same inlet CO_2 pressure (0.10 kPa) and 0.52 (solid), 1.0 (dashed), 2.1 (dash-dotted), and 4.1 (dotted) kPa CO. (b) Reactions performed with the same inlet CO pressure (2.1 kPa) and 0.045 (dotted), 0.10 (dash-dotted), 0.20 (dashed), and 0.40 (solid) kPa CO_2.

The strong effects of ξ_{red} on k_{app} (Figure 3b) indicates that changes in the solvent with O* content influence the stability of O* and the TS to different extents ($\Delta G^{E,\ddagger}_{app} \neq 0$; $\Delta G^{E,\ddagger}_{app}$ is a function of ξ_{red}). The same solvation effects that lead to the preferential stabilization of O* versus * with increasing ξ_{red} for the redox thermodynamic data (Figure 2 and eq 7) also affect the solubilities of O*, TS, and other solutes that are present during CZO stoichiometric reduction reactions.

The term within the large square brackets in eq 9 equals k_{app} (eq 8) when the elementary reaction of CO with O* is the sole kinetically relevant step for CZO reduction by CO and bare oxygen anions (not covered by any bound species, such as CO or CO_2) are the most abundant species at CZO surfaces. In addition, the reverse reaction (CZO oxidation by CO_2) must proceed much more slowly than the forward reaction for measured net CO_2 formation rates (r_{CO_2}) to solely reflect CZO reduction by CO. In other words, the reduction reaction must be far away from equilibrium at all conditions. The approach to equilibrium for CZO reduction (η) is defined as the ratio of oxidation to reduction rates ($\eta = r_{ox}/r_{red}$):

$$r_{CO_2} = r_{red}(1 - \eta) \tag{10}$$

and can be expressed in terms of the thermodynamic metrics (eqs 4–6) for the O_2 evolution reaction (eq 3):

$$\eta = \left[\exp\left(\frac{\Delta G^{\ominus}_{c,CO} + \frac{1}{2}\Delta G_{red}}{RT}\right)\right]\left(\frac{P_{CO_2}}{P_{CO}}\cdot\frac{\xi_{red}}{1 - \xi_{red}}\right) \tag{11}$$

where $\Delta G^{\ominus}_{c,CO}$ is the Gibbs free energy of CO combustion (per mol of CO) at standard conditions. Measured r_{CO_2} values are equal to the forward CZO reduction rates (r_{red}) only when η is much smaller than unity. These prerequisites regarding the identity of the kinetically relevant step, the presence of additional "solutes" besides O* on CZO surfaces, and the approach to equilibrium must be verified with kinetic and mechanistic evidence (*vide infra*) before "solvation effects" on rates can be attributed to solubility changes for the kinetically relevant solutes as O* is removed from the CZO crystal lattice.

The strong effects of ξ_{red} on ΔG^{E}_{red} and $\Delta G^{E,\ddagger}_{app}$ (Figures 2 and 3b) must be considered in interpreting results through mathematical descriptions, because even weak axial gradients in [O*] (= $(1 - \xi_{red})$) would strongly influence CO_2 formation rates. In most instances, experiments can be designed and conditions chosen to allow rate measurements that are only weakly affected by reactant depletion or product accumulation for a given bed residence time. For the system at-hand, the severe thermodynamic nonidealities lead to O atom removal rates that decrease 2-fold as O* concentrations only slightly decrease (e.g., by 1.1-fold; ξ_{red} increases from 0 to 0.1; Figure 3). This requires data analysis using reaction-convection mole balances in order to capture the temporal and spatial gradients in reactant and product pressures and solute concentrations as CZO reduction reactions proceed. A cursory assessment of the effects of CO and CO_2 pressures and extents of reduction on k_{app} and η values can still provide preliminary insight into kinetic dependencies and reaction reversibility that guide the development of accurate rate equations and rigorous reaction-convection models.

Figure 4a shows k_{app} values (eq 8) at different ξ_{red} values (eq 2) for $Ce_{0.5}Zr_{0.5}O_2$ reduction at 0.52 (solid), 1.0 (dashed), 2.1 (dash-dotted), and 4.1 (dotted) kPa CO and 648 K and the same inlet CO_2 pressure (0.10 kPa). The apparent first-order rate constants increase with increasing CO pressure at all extents of reduction, but not with strictly proportional trends with CO pressure. For example, at a ξ_{red} of 0.1, k_{app} increases linearly from 0.52 to 1.0 kPa CO, but sublinearly at higher CO pressures. These deviations from first-order CO kinetics do not reflect CO depletion from the reactant stream (fractional CO conversions were less than 0.08) or detectable coverages of CO at O* surface sites (CO does not bind to $Ce_{0.5}Zr_{0.5}O_{2-x}$ surfaces; *vide infra*, Sections 3.3 and 3.4). They arise instead from axial bed gradients in ξ_{red} and CO_2 pressures, which become more prevalent as rates increase with increasing CO pressure. Figure 4b shows profiles analogous to those in Figure 4a but for reactions performed with an inlet CO pressure of 2.1 kPa and different inlet CO_2 pressures (0.045, dotted curve; 0.10, dash-dotted; 0.20, dashed; and 0.40 kPa, solid). These k_{app} values decrease with increasing CO_2 pressure at all ξ_{red} values. Such trends confirm the inhibition of CZO reduction rates through competitive adsorption of CO_2-derived species on surface redox sites; they can also be the result of a closer approach to equilibrium for this reaction (eqs 10 and 11) at

https://doi.org/10.1021/acscatal.4c04771
ACS Catal. 2024, 14, 16184−16204

higher CO_2 pressures, a possibility discarded by assessments of reaction reversibility (*vide infra*).

Reduction−oxidation thermodynamic data at 873 K (Figures 1 and 2) cannot be used to obtain approach to equilibrium values (η, eq 11) at the lower temperatures (648 K) used to measure reduction rates, chosen here to match conditions typical of "cold start" in emissions control,[21−23] because ΔG_{red} values and their dependence on ξ_{red} depend on temperature and on the structural and morphological properties that are specific to any given $Ce_{0.5}Zr_{0.5}O_{2-x}$ sample. Thus, attempts to acquire thermodynamic data at 648 K were made using the same protocols used at 873 K (Figures 1 and 2) to assess whether the CO_2 effects on O atom removal rates (Figure 4b) reflect kinetic or thermodynamic origins. The data in Figure 5 are analogous to those shown in Figure 1, but for

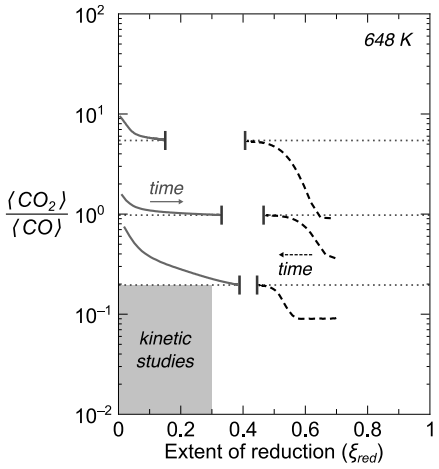

Figure 5. Ratio of average CO_2 and CO pressures ($\langle CO_2\rangle/\langle CO\rangle$) versus extent of reduction (ξ_{red}) for $Ce_{0.5}Zr_{0.5}O_2$ reduction (solid) and $Ce_{0.5}Zr_{0.5}O_{1.82}$ oxidation (dashed) reactions conducted at 648 K and using reactant streams with (CO, CO_2) pressures of (0.18, 1.0), (1.0, 1.0), and (1.0, 0.20) kPa.

$Ce_{0.5}Zr_{0.5}O_{2-x}$ reduction (solid) and oxidation (dashed) at 648 K (instead of 873 K) using CO−CO_2 mixtures that give virtual O_2 pressures of 1.3×10^{-34} (CO_2/CO = 0.20), 3.1×10^{-33} (0.98), and 9.6×10^{-32} bar (5.5). In contrast with the data at 873 K (Figure 1), the $\langle CO_2\rangle/\langle CO\rangle$ values at 648 K do not converge with time to the same final ξ_{red} value when starting either from the stoichiometric oxide ($Ce_{0.5}Zr_{0.5}O_2$, $\xi_{red,0} = 0$; solid curves) or from $Ce_{0.5}Zr_{0.5}O_{1.82}$ ($\xi_{red,0} \approx 0.7$; dashed curves). Thus, equilibrium is not attained at the end of the reduction or oxidation processes. Kinetic hurdles for O atom removal/addition become insurmountable as either reaction proceeds, leading to undetectable levels of O atom removal or addition (and of CO_2/CO formation) before equilibrium can be achieved.

These attempts to measure reduction−oxidation equilibria did, however, define a range of possible equilibrium ξ_{red} values for each CO_2/CO ratio at 648 K, as depicted by the regions between the terminal extents of reduction for the CZO reduction (solid) and oxidation (dashed) traces (Figure 5); the terminal ξ_{red} values are emphasized with the three pairs of vertical bars. This range was determined by considering that the equilibrium ξ_{red} values must be the same when reached by reduction or oxidation processes at a given virtual O_2 pressure (as it does at 873 K; Figure 1). The CO_2/CO ratios and extents of reduction (ξ_{red}) in these kinetic studies (Figures 3 and 4) are denoted by the shaded region in the bottom left corner of Figure 5. The largest ξ_{red} value achieved in stoichiometric reduction measurements at 648 K is 0.30 (for $\langle CO_2\rangle/\langle CO\rangle$ = 0.23). An equilibrium ξ_{red} value of 0.30 would have required much larger CO_2/CO ratios (>2). Thus, the maximum possible value for approach to equilibrium (η, eq 11) that could have been attained in these kinetic studies is approximately 0.1. This small value for the upper bound of η implies that measured net CO_2 formation rates reflect forward CZO reduction rates; in other words, $(1-\eta)$ is approximately equal to 1 (eq 10). The observed decrease in k_{app} with increasing CO_2 pressure (Figure 4b) can then be attributed solely to kinetic inhibition.

The first-order dependence in CO (Figure 4a) suggests that stoichiometric O atom removal proceeds through a kinetically relevant TS that contains one CO molecule and one O atom, and the observed inhibition effects by CO_2 (Figure 4b) show, in turn, that $Ce_{0.5}Zr_{0.5}O_{2-x}$ surfaces contain kinetically detectable coverages of CO_2-derived species. These observed kinetic trends can likely be captured with the following functional form for the stoichiometric reduction rate equation ($\hat{r}_{stoich}$):

$$\hat{r}_{stoich} = \alpha P_{CO}[O^*] = \frac{\alpha P_{CO}}{1 + \beta P_{CO_2} + \omega \frac{[*]}{[O^*]} P_{CO_2}} \quad (12)$$

The above rate equation (eq 12) is expressed as a function of the solute concentrations ([*] and [O*]) instead of thermodynamic activities because they are directly measurable in experiments as ξ_{red} (eq 2; Figures 1−4). As a result, the parameters (α, β, and ω) represent lumped rate and equilibrium constants for elementary steps, and they include all relevant nonidealities and solvation effects for the species involved in such steps. Scheme 1 depicts a plausible

Scheme 1. Elementary Step Sequence for Stoichiometric Reduction of $Ce_{0.5}Zr_{0.5}O_{2-x}$ by CO

$$CO + O^* \xrightarrow{\alpha} CO_2 + *$$
$$CO_2 + O^* \underset{0}{\overset{\beta}{\rightleftharpoons}} CO_3^*$$
$$CO_2 + * \underset{0}{\overset{\omega}{\rightleftharpoons}} CO_2^*$$

mechanism that tentatively assigns chemical meaning to α, β, and ω. In this Scheme, CO reacts with surface O-anions (O*; present in equilibrium with the bulk $Ce_{0.5}Zr_{0.5}O_{2-x}$) in the sole kinetically relevant step (α) and CO_2 binds competitively to surface O-anions (β) and/or anion vacancies (*; ω) to form carbonate (CO_3*) and carboxylate (CO_2*) solutes that inhibit O atom removal rates by occupying surface redox sites. The terms in the denominator of $\hat{r}_{stoich}$ (eq 12) reflect the relative coverages of, from left to right, O*, CO_3*, and CO_2*.

The tenets of transition state theory can be applied to the irreversible O-atom removal step (α, Scheme 1) and the quasi-equilibrium approximation to the two CO_2 adsorption steps (β and ω), leading to relationships between activity coefficients and (excess) free energy changes for the parameters in $\hat{r}_{stoich}$ (eq 12):

https://doi.org/10.1021/acscatal.4c04771
ACS Catal. 2024, 14, 16184−16204

$$\alpha = \alpha_{\ominus} \cdot \frac{\gamma_{O^*}}{\gamma_{TS}} = \exp\left(-\frac{\Delta G_{\alpha}^{\ominus,\ddagger} + \Delta G_{\alpha}^{E,\ddagger}}{RT}\right) \quad (13)$$

$$\beta = \beta_{\ominus} \cdot \frac{\gamma_{O^*}}{\gamma_{CO_3^*}} = \exp\left(-\frac{\Delta G_{\beta}^{\ominus} + \Delta G_{\beta}^{E}}{RT}\right) \quad (14)$$

$$\omega = \omega_{\ominus} \cdot \frac{\gamma_{*}}{\gamma_{CO_2^*}} = \exp\left(-\frac{\Delta G_{\omega}^{\ominus} + \Delta G_{\omega}^{E}}{RT}\right) \quad (15)$$

where $\chi_{\ominus}$ ($\chi = \alpha$, β, and ω) represents rate (α) or equilibrium (β and ω) constants for the elementary steps in Scheme 1 and γ_j denotes the activity coefficients for each solute (j = O*, *, TS, CO_3*, and CO_2*). These $\chi_{\ominus}$ values reflect free energy changes for the ideal-solution reference condition ($\Delta G_{\chi}^{\ominus}$); the excess free energy changes (ΔG_{χ}^{E}) account, in turn, for any thermodynamic nonidealities. The reduction−oxidation thermodynamic data in Figure 2 shows that deviations from ideal thermodynamics are accurately represented by single-valued functions of ξ_{red}. Free energy scaling relations would then imply that changes in the relative solubilities of TS, CO_3*, and CO_2* solutes can also be expressed as single-valued functions of ξ_{red}:

$$\chi = \chi_{\ominus} + \chi_1 \cdot \xi_{red}^{\ 1} + \chi_2 \cdot \xi_{red}^{\ 2} + \cdots \approx \chi_{\ominus} + \chi_1 \cdot \xi_{red}^{\ 1} \quad (16)$$

Retaining the first two terms in the expansion is equivalent to considering linear scaling relations between ΔG_{χ}^{E} and ΔG_{red}^{E} which when combined with the linear dependence of ΔG_{red}^{E} on ξ_{red} (Figure 2 and eq 7) give α, β, and ω also as single-valued functions of ξ_{red}:

$$\alpha = \alpha_{\ominus} \exp(m_{\alpha} \cdot \xi_{red}) \quad (17)$$

$$\beta = \beta_{\ominus} \exp(m_{\beta} \cdot \xi_{red}) \quad (18)$$

$$\omega = \omega_{\ominus} \exp(m_{\omega} \cdot \xi_{red}) \quad (19)$$

The stoichiometric reduction rate equation ($\hat{r}_{stoich}$, eq 12) depends on three parameters that characterize the ideal solution ($\chi_{\ominus}$) and three parameters that capture the consequences of thermodynamic nonidealities (m_{χ}) as ξ_{red} increases.

This mechanistic proposal (Scheme 1) and the linear scaling relations (eqs 17−19) used to describe the nonideal character of CZO reduction−oxidation cycles can be assessed by comparing rate data (Figure 4) with the predictions from the functional form of $\hat{r}_{stoich}$ (eq 12). This computational task requires nonlinear regression techniques and numerical methods for solving stiff partial differential equations. Taken together with the six parameters in eqs 12 and 17−19, these methods are likely to give large uncertainties or significant covariance in the parameter estimates. What follows seeks to decrease the number of parameters and to provide independent confirmation for the steps in Scheme 1 and for the derived rate equation ($\hat{r}_{stoich}$, eq 12). This is achieved by assessing the kinetics and mechanism of CZO reduction for the infinitely dilute solution ($\xi_{red} \to 0$), a system that fortuitously prevails at the conditions of catalytic CO oxidation reactions, during which O* is consumed by CO are replenished by O_2 at conditions of pseudo steady-state.

3.3. Kinetics and Mechanism of Catalytic CO Oxidation on $Ce_{0.5}Zr_{0.5}O_2$.

A kinetic analysis of steady-state CO oxidation catalysis on $Ce_{0.5}Zr_{0.5}O_{2-x}$ provided complementary mechanistic insights into the transient stoichiometric process. The collection and interpretation of these data are more straightforward than those for the transient process because steady-state reaction-convection models involve gradients in reactant and product concentrations only along the axial dimension of the bed, thus avoiding the stiff partial differential equations required to account for the temporal and spatial evolution in transient systems. Moreover, catalytic rates can be measured at conditions that ensure essentially stoichiometric O* concentrations, which can be confirmed by rates being independent of O_2 pressure. This avoids the strong effects of ξ_{red} on rates and allows for independent assessment of the rate and equilibrium constants ($\chi_{\ominus}$; eqs 17−19) for the "ideal solution" ($Ce_{0.5}Zr_{0.5}O_2$; $\xi_{red} \to 0$), thus decreasing, in theory, the number of parameters in eq 12 from six to three.

Catalytic oxidations on reducible oxides proceed via Mars-van Krevelen redox cycles, in which O-atoms within metal oxides are removed by the substrate and restored by a source of O-atoms (e.g., O_2, CO_2, H_2O, N_2O).[45−47] Scheme 2 depicts a generic form of such cycles for aerobic CO oxidation at two-electron redox centers exposed at surfaces of reducible oxides. CO reacts with oxygen anions (O*) to form CO_2, O_2 binds at anion vacancies (*) to form a bound dioxygen intermediate (O_2*), and CO consumes one of the O-atoms in O_2* to close the catalytic cycle. The O* removal step occurs in both the catalytic (Scheme 2) and stoichiometric reduction (Scheme 1) reactions on $Ce_{0.5}Zr_{0.5}O_2$, and the observed near first-order CO dependence for the latter (Figure 4a) suggests that it is the kinetically relevant one in transient stoichiometric reduction processes.

Scheme 2. Mars-van Krevelen Redox Cycle for Aerobic CO Oxidation

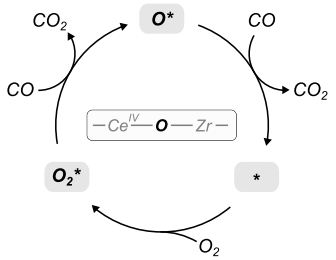

Figure 6 shows CO_2 formation rates at each time ($r_{CO_2}(t)$) normalized to that for steady-state catalytic CO−O_2 reactions (648 K, 1.1 kPa CO, 0.21 kPa CO_2; $r_{CO_2}^{st.-st.}$) during an experiment in which the O_2 inlet pressure was abruptly switched from 4.0 to 0 kPa. The time covered by the dotted line between 0 and 0.030 ks represents a linear extrapolation (in semilogarithmic scale) of anaerobic rates during a time period affected by short hydrodynamic delays, as evident from the evolution of inert Ar tracer concentrations. CO_2 formation rate decreased abruptly by about a factor of 2 upon removing O_2 from the inlet stream:

$$r_{CO_2}(t \to 0) \approx (1/2) \cdot r_{CO_2}^{st.-st.}$$

https://doi.org/10.1021/acscatal.4c04771
ACS Catal. 2024, 14, 16184−16204

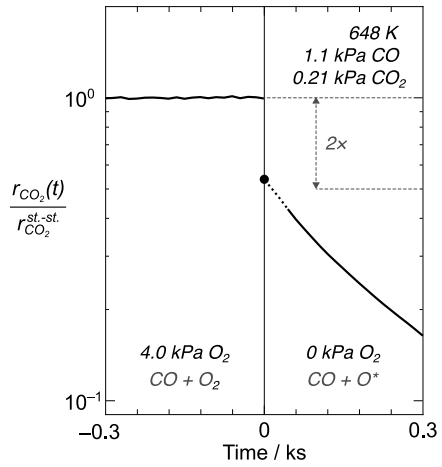

Figure 6. Normalized CO_2 formation rate versus time (t) for CO oxidation on $Ce_{0.5}Zr_{0.5}O_2$ (648 K, 1.1 kPa CO, 0.21 kPa CO_2). At t = 0 ks, the reactant stream was abruptly switched from aerobic (4.0 kPa O_2) to anaerobic conditions. CO_2 formation rates ($r_{CO_2}(t)$) are normalized to the steady-state CO_2 formation rate during aerobic CO oxidation catalysis ($r_{CO_2}^{st.-st.}$). The dotted line represents estimates of CO_2 rates, determined via linear extrapolation on a semilogarithmic scale, at early times after switching to anaerobic conditions in which the acquired data were corrupted by a brief hydrodynamic delay (30 s).

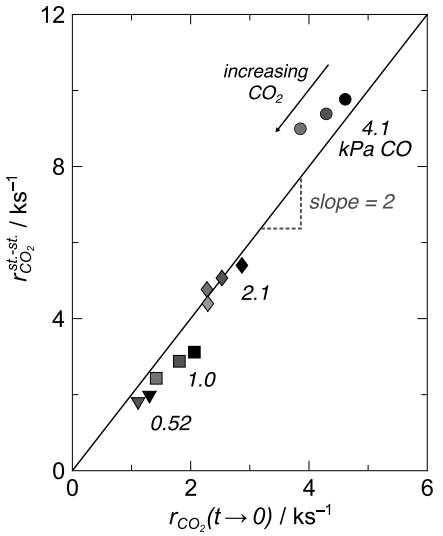

Figure 7. Steady-state CO_2 formation rates during CO oxidation catalysis on $Ce_{0.5}Zr_{0.5}O_2$ ($r_{CO_2}^{st.-st.}$) versus initial CO_2 formation rates in stoichiometric reduction of $Ce_{0.5}Zr_{0.5}O_2$ by CO ($r_{CO_2}(t \to 0)$) at 648 K. The triangles, squares, diamonds, and circles represent experiments at 0.52, 1.0, 2.1, and 4.1 kPa CO, respectively, and an increase in the lightness of the symbol shading reflects an increase in CO_2 pressure (0.045−0.40 kPa). The solid parity line has a slope of 2.

Catalytic CO oxidation turnovers form two CO_2 molecules for each O* consumed (with the other O-atom being consumed in converting O_2* to O*; Scheme 2) while stoichiometric $Ce_{0.5}Zr_{0.5}O_2$ reduction forms one CO_2 per O* (Scheme 1):

$$r_{cat} = (1/2)\cdot r_{CO_2}^{st.-st.}$$

$$r_{stoich}(t) = r_{CO_2}(t)$$

Thus, the abrupt 2-fold decrease in CO_2 formation rate shows that the rate of steady-state catalytic CO oxidation (r_{cat}) is equal to the initial rate in stoichiometric $Ce_{0.5}Zr_{0.5}O_2$ reduction by CO ($r_{stoich}(t \to 0)$) at this condition (648 K, 1.1 kPa CO, and 0.21 kPa CO_2). This implies that r_{cat} and $r_{stoich}(t \to 0)$ reflect the same kinetically relevant step, which must be the O* removal step since it is the only one that occurs in both catalytic (Scheme 2) and stoichiometric (Scheme 1) elementary step sequences.

Figure 7 shows a comparison between steady-state CO_2 formation rates during CO oxidation catalysis ($r_{CO_2}^{st.-st.}$) and initial CO_2 formation rates during stoichiometric reduction of $Ce_{0.5}Zr_{0.5}O_2$ by CO ($r_{CO_2}(t \to 0)$); each point represents a comparison at the same inlet CO and CO_2 pressures. The catalytic rate remains 2-fold higher than initial stoichiometric rates at all conditions (648 K, 0.52−4.1 kPa CO, 0.045−0.40 kPa CO_2), demonstrating that the reaction between CO and O* is the sole kinetically relevant step in both catalytic and stoichiometric processes. The initial state of $Ce_{0.5}Zr_{0.5}O_{2-x}$ during the transient reactions is the stoichiometric oxide ($Ce_{0.5}Zr_{0.5}O_2$; $\xi_{red,0} = 0$). Thus, these results set the expectation that the catalytic rate data can be described by a rate equation ($\hat{r}_{cat}$) with a functional form that is identical to that for the stoichiometric reaction ($\hat{r}_{stoich}$, eq 12), but for conditions in which ξ_{red} asymptotically approaches zero:

$$\hat{r}_{cat} = \lim_{\xi_{red}\to 0} \hat{r}_{stoich} = \frac{\alpha_{cat} P_{CO}}{1 + \beta_{cat} P_{CO_2} + \omega_{cat} \frac{P_{CO}}{P_{O_2}} P_{CO_2}} \quad (20)$$

The parameters in eq 20 (α_{cat}, β_{cat}, and ω_{cat}) are rate and equilibrium constants for the steps in Scheme 1; they include the ideal-solution component ($\chi_{\ominus}$, eqs 13−15) and any contributions from thermodynamic nonidealities that may emerge during CO oxidation catalysis. The rightmost term in the denominator of $\hat{r}_{cat}$ (eq 20) represents, as in the case of $\hat{r}_{stoich}$ (eq 12), the ratio of carboxylate (CO_2*) to oxygen anion (O*) surface coverages; here, pseudo steady-state balances on reaction intermediates (O*, *, and O_2*) lead to ratios of reduced to oxidized ([*]/[O*]) centers being strictly proportional to the ratio of CO to O_2 pressures. Thus, a kinetic study of CO oxidation catalysis can lend independent evidence supporting the mechanistic proposal for the stoichiometric reaction (Scheme 1) and regression of such data to the functional form of eq 20 can provide parameters estimates for the ideal-solution components to α, β, and ω (eqs 12 and 17−19).

Figure 8a, b, and c show the effects of O_2, CO, and CO_2 pressures, respectively, on catalytic CO oxidation rates. The abscissa values are inlet−outlet averages of these pressures (denoted as $\langle O_2 \rangle$, $\langle CO \rangle$, and $\langle CO_2 \rangle$). Rates were insensitive to O_2 pressure (Figure 8a), indicative of catalytic reactions that occur on CZO surfaces predominantly occupied by O* (ξ_{red} = 0) through kinetically inconsequential O_2 activation steps, as typically observed in Mars-van Krevelen redox cycles.[46,48] Measured rates are strictly proportional to CO at sufficiently high inlet CO_2 pressures (>0.80 kPa), which dampen any axial CO_2 gradients caused by the catalytic reaction ($\langle CO_2 \rangle$ = 0.85−0.97 kPa; diamonds, Figure 8b). Rates deviate significantly from the linear CO dependence (dashed lines) at low inlet

https://doi.org/10.1021/acscatal.4c04771
ACS Catal. 2024, 14, 16184−16204

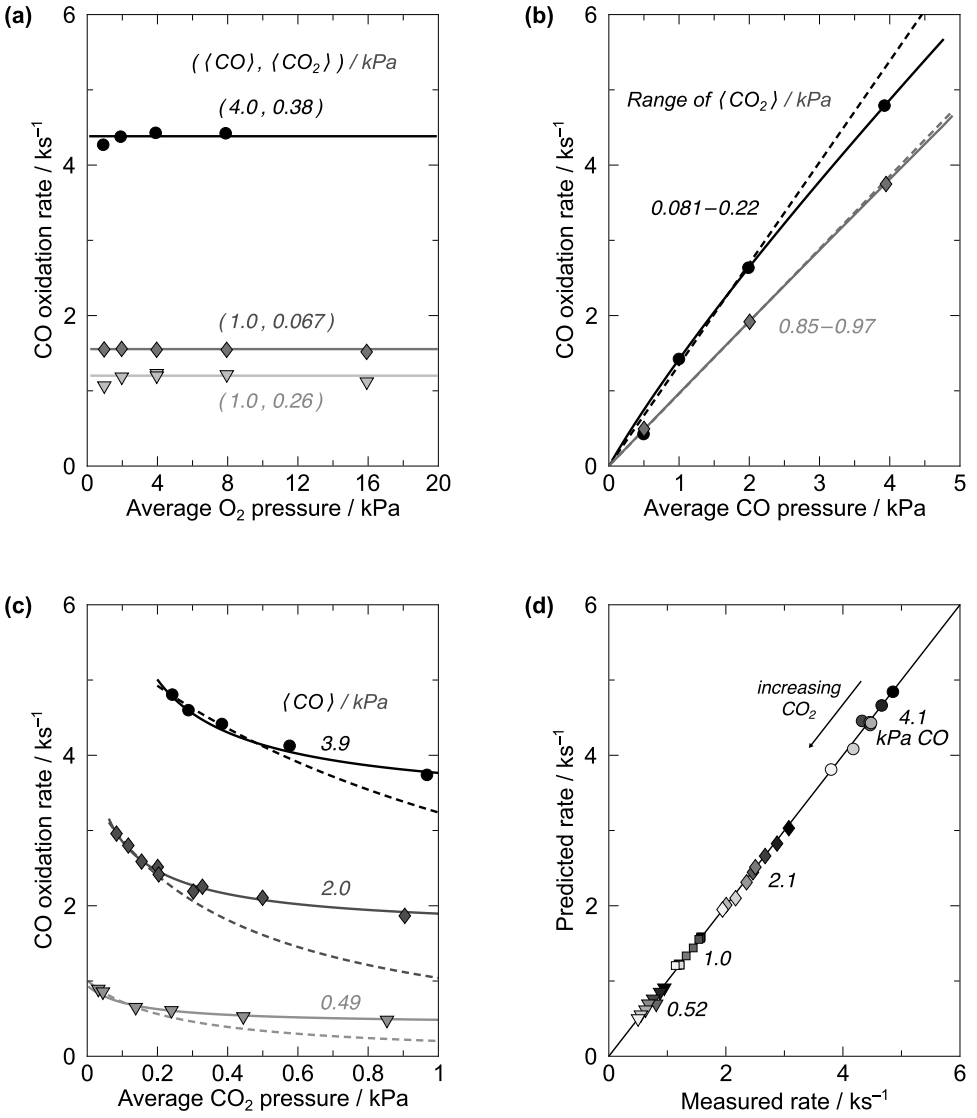

Figure 8. (a–c) Catalytic CO oxidation rates on $Ce_{0.5}Zr_{0.5}O_2$ at 648 K versus average O_2 (a), CO (b), and CO_2 (c) pressures. The solid curves are predictions for the kinetic trends made using an integral reactor model with eq 21 for the rate equation (r_{cat}) and the best-fit values of the rate parameters (eqs 22–24). (d) Parity plot of predicted versus measured rates. The triangles, squares, diamonds, and circles represent values with, respectively, 0.52, 1.0, 2.1, and 4.1 kPa CO in the reactant mixtures, and for each symbol shape, the increased lightness of the shading reflects an increase in average CO_2 pressure, spanning 0.032 to 0.97 kPa CO_2.

CO_2 pressures (0.045 kPa; circles, Figure 8b) when axial CO_2 gradients become appreciable, as reflected by $\langle CO_2 \rangle$ values being significantly larger than the inlet CO_2 pressure ($\langle CO_2 \rangle / (CO_2)_{in}$ = 1.8–4.9). The first-order dependence overpredicts rates at the highest CO pressure when the rate, and thus the prevailing CO_2 pressure, is largest, indicative of competitive adsorption by CO_2. These O_2 and CO dependencies as well as the observed product inhibition are consistent with the functional form of the proposed rate equation (eq 20).

Rates decreased with increasing average CO_2 pressures (Figure 8c), indicative of detectable coverages of bound CO_2-derived species on redox sites exposed at CZO surfaces. Such species must be carbonates (formed by CO_2 binding to O*; CO_3*), because CO oxidation rates are independent of O_2 pressure; the β term in eq 20 reflects the ratio of CO_3* to O* coverages. Kinetically consequential coverages of surface carboxylates (formed by CO_2 binding to *; CO_2*) during CO oxidation catalysis at 648 K, reflected by the ω term in the denominator of eq 20, would manifest as positive-order O_2 and sublinear CO dependencies, which is inconsistent with the observed O_2 and CO trends (Figure 8a,b). Thus, the most abundant species on CZO surfaces during CO–O_2 reactions consist of O* with and without bound CO_2 (CO_3*). Steady-state CO oxidation rates that are twice the initial stoichiometric rates for CZO reduction by CO (Figures 6 and 7) are also evidence of * and CO_2* species contributing negligibly to surface site balances during oxidation catalysis, because [*]/[O*] ratios are essentially zero during the initial stage of the transient reduction reactions ($Ce_{0.5}Zr_{0.5}O_2$, $\xi_{red,0}$ = 0).

The functional form of eq 20 ($\hat{r}_{cat}$), which attributes the CO_2 effects solely to competitive adsorption, cannot fully capture the observed CO_2 dependencies (Figure 8c). This equation would give CO oxidation rates that decrease monotonically with increasing CO_2 pressure (as shown by the dashed curves) and ultimately must approach zero at high enough CO_2 pressures. Instead, measured rates become insensitive to CO_2 at high CO_2 pressures. This suggests that the prevalence of

https://doi.org/10.1021/acscatal.4c04771
ACS Catal. 2024, 14, 16184–16204

CO_3* adsorbates leads to the preferential stabilization of kinetically relevant O-atom removal transition states and/or to the destabilization of O* reactants, thereby compensating for the kinetic inhibition caused by O* site blocking. In other words, high coverages of CO_3* at $Ce_{0.5}Zr_{0.5}O_2$ surfaces (ξ_{red} = 0) lead to intrinsic O-atom removal rates (reflected by the α term in eq 20) that exceed those on bare stoichiometric surfaces ($\alpha_\ominus$; eq 17). Effectively, $Ce_{0.5}Zr_{0.5}O_2$ particles become more "oxidized" as CO_3* coverages increase, leading to apparent "negative extents of reduction" and α values greater than that for the "ideal solution" reference condition ($\alpha > \alpha_\ominus$). The kinetic data (Figure 8a−c) can be accurately described by an integral reactor model with the following expression for the catalytic CO oxidation rate equation (r_{cat}):

$$r_{cat} = \frac{\alpha_{cat} P_{CO}}{1 + \beta_{cat} P_{CO_2}} = \frac{[\alpha_\ominus (1 + \lambda P_{CO_2})] P_{CO}}{1 + \beta_\ominus P_{CO_2}} \quad (21)$$

The λP_{CO_2} term in the numerator of eq 21 reflects the CO_3* induced nonidealities on α (*vide infra*). Figure 8d shows predicted and measured rates in a parity plot, and the solid curves in Figure 8a−c represent model predictions using an integral reactor model (Section S3; SI). The regressed $\alpha_\ominus$, $\beta_\ominus$, and λ parameters and their uncertainties (95% confidence intervals) are

$$\alpha_\ominus = (3.9 \pm 0.4)\ \text{kPa}^{-1}\ \text{ks}^{-1} \quad (22)$$

$$\beta_\ominus = (8.1 \pm 3.4)\ \text{kPa}^{-1} \quad (23)$$

$$\lambda = (3.6 \pm 1.4)\ \text{kPa}^{-1} \quad (24)$$

from a minimization of the relative error between predicted and measured CO_2 yields (Section S3; SI).

The $\alpha_\ominus$ and $\beta_\ominus$ parameters in eq 21 reflect the Gibbs free energies of formation of the O-atom removal TS ($\Delta G_\alpha^{\ominus,\ddagger}$, eq 13) and of CO_3* species ($\Delta G_\beta^\ominus$, eq 14) for the "ideal solution", consisting of the stoichiometric oxide ($Ce_{0.5}Zr_{0.5}O_2$, ξ_{red} = 0) without any guest molecules bound to its surface. The λP_{CO_2} term in the numerator of r_{cat} (eq 21) can be attributed to solvation effects on O-atom removal transition states induced by the presence of surface-bound carbonates, akin to those induced by changes in ξ_{red} but in the opposite direction (eqs 16 and 17):

$$\alpha = \alpha_\ominus + \alpha_1 \cdot \xi_{red} + \cdots = \alpha_\ominus (1 + \lambda P_{CO_2}) + \alpha_1 \cdot \xi_{red} + \cdots \quad (25)$$

CO_2 acts as an electron acceptor (Lewis acid) when bound at basic O* centers at oxide surfaces;[49] such binding can alter the bulk electronic properties of semiconducting oxides, as shown by changes in band gap energies upon adsorption of various electron donor and acceptor molecules onto TiO_2 surfaces.[50] Thus, CO_3* withdraws electron density from $Ce_{0.5}Zr_{0.5}O_2$ crystals. The fast lattice diffusion within such crystals causes changes in bulk electronic properties induced by guest molecule sorption to uniformly affect the reactivity and binding properties of each solute within the "well-mixed" solution.

In the stoichiometric reactions, the strong decrease in k_{app} values (eq 8) with increasing ξ_{red} (Figures 3 and 4) reflects, in part, O-atom removal transition states that become increasingly destabilized relative to O* reactants as CZO crystals become increasingly reduced. These effects of ξ_{red} can instead be articulated in terms of solution electron density, which decreases as O-atoms are added, Ce(III) cations are oxidized, and electrons become localized to form Ce−O and Zr−O bonds. The bulk electron density within $Ce_{0.5}Zr_{0.5}O_2$ crystals (ξ_{red} = 0) also decreases as the surface coverage of CO_3* increases, leading to CO_2-covered crystals that are more "oxidized" than bare ones. Directionally, this "overoxidation" results in O-atom removal transition states becoming more stable and O* reactants less stable as CO_3* coverages on $Ce_{0.5}Zr_{0.5}O_2$ increase. The λP_{CO_2} term in eq 25 represents a linearization of these CO_3* coverage effects on α, which attenuates the kinetic inhibition of O-atom removal rates that arises from O* site blocking ($\beta_\ominus P_{CO_2}$ in r_{cat}, eq 21). This coverage effect re-emphasizes the profound consequences of thermodynamic nonidealities on surface reaction dynamics; they manifest even for the ideal solution of $Ce_{0.5}Zr_{0.5}O_2$ crystals that are infinitely diluted in anion vacancies ($\xi_{red} \to 0$).

The interpretation of CO oxidation kinetics described in this section provided corroborating mechanistic evidence for the stoichiometric reduction reaction. CO-mediated O-atom removal is the sole kinetically relevant step and CO_2 binds to oxygen anions to form appreciable coverages of surface carbonates during both stoichiometric and catalytic CO oxidation. These results also decrease the number of free parameters by two, since the estimated values of $\alpha_\ominus$ and $\beta_\ominus$ (eqs 22 and 23) are applicable to the catalytic and the stoichiometric reactions, as indicated by the good agreement between initial stoichiometric and steady-state catalytic rates (Figures 6 and 7). The rate equation for the stoichiometric reaction must include the term that accounts for the CO_3* coverage effects on α (i.e., $(1 + \lambda P_{CO_2})$ in eqs 21 and 25). Also, an accurate description of stoichiometric rate data will likely require the retention of terms that reflect the relative coverages of * and/or CO_2*, which were kinetically inconsequential in catalytic CO−O_2 reactions, because the concentrations of anion vacancies become appreciable as stoichiometric reduction of CZO proceeds.

3.4. Desorption and Decomposition of CO_2-Derived Surface Species on $Ce_{0.5}Zr_{0.5}O_{2-x}$. Binding energies derived from density functional theory calculations for CO_2 on $Ce_{21}O_{41}$ and $Ce_{21}O_{42}$ particles[51] and $CeO_2(110)$ surfaces with and without anion vacancies[52] indicate that CO_2 binds more strongly onto vacancies than on O-anions. Temperature ramping experiments in ultrahigh vacuum systems involving CO_2-dosed (5 Langmuirs at 180 K) $CeO_{1.7}(100)$ and $CeO_2(100)$ films showed that the amount of CO_2 evolved was about 1.5 times larger and the temperature required to fully desorb CO_2 was significantly higher (850 K vs 700 K) when heating partially reduced versus stoichiometric samples,[53] consistent with CO_2-derived adsorbates being more stable when bound at reduced (*) versus oxidized centers (O*). This section reports evidence that extends these conclusions to $Ce_{0.5}Zr_{0.5}O_{2-x}$ and which supports the hypothesis, based on the observed kinetic inhibition of CZO reduction rates by CO_2 (Figure 4b), that terms for both CO_3* and CO_2* coverages must be retained in surface site balances for the stoichiometric reaction rate equation (eq 12).

https://doi.org/10.1021/acscatal.4c04771
ACS Catal. 2024, 14, 16184−16204

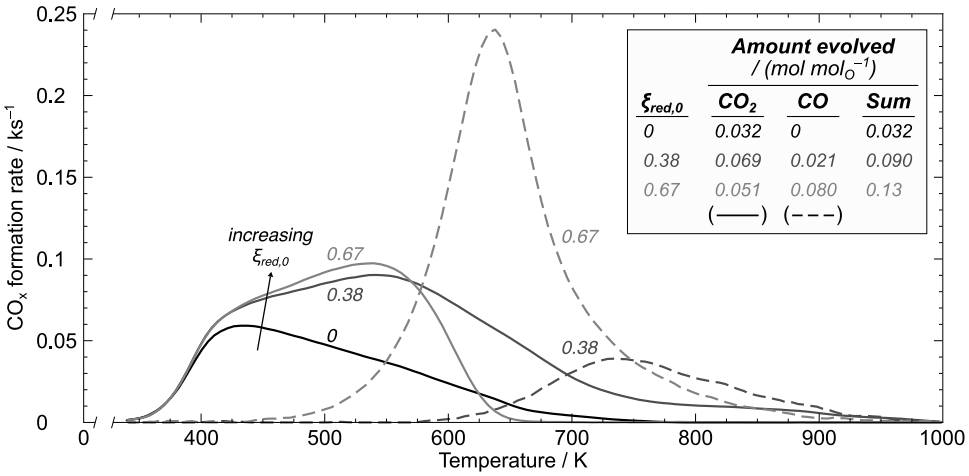

Figure 9. CO_2 (solid) and CO (dashed) formation rates while heating (0.33 K s^{-1}), in a flowing inert stream, CO_2-treated $Ce_{0.5}Zr_{0.5}O_{2-x}$ samples with initial extents of reduction ($\xi_{red,0}$) of 0 (black), 0.38 (dark-gray), and 0.67 (light-gray).

In our study, stoichiometric $Ce_{0.5}Zr_{0.5}O_2$ crystals ($\xi_{red,0}$ = 0) were exposed to CO_2 (2.0 kPa in He) in a flowing stream at 340 K and the powder was flushed with He and heated to 1000 K (at 0.33 K s^{-1}) also in flowing He. The solid black curve in Figure 9 shows the CO_2 evolution rates during this process. CO_2 starts to evolve at 350 K, reaches a maximum rate at 430 K, and becomes undetectable above 750 K. The amount of CO_2 evolved corresponds to 0.032 molecules (per removable O-atoms in CZO), a value that is 0.4 ML of O-atoms (a monolayer, ML, corresponds to 0.081, 0.10, or 0.14 mol mol_O^{-1} for cubic CZO crystals (40 m^2 g^{-1}, a = 0.52909 nm that expose only (111), (110), and (100) facets, respectively). This result shows that CO_2 can bind to O-anions as carbonates (CO_2 + O* → CO_3*) at 340 K and that such species desorb between 350 and 750 K.

The CO_2 evolution rates in Figure 9 cannot be accurately described using a first-order Langmuirian model for CO_3*, which would give much sharper than observed decreases in rate after the maximum value. Second-order desorption improves marginally the agreements, but it is not chemically plausible. The apparent reaction order being greater than one for this unimolecular step instead reflects a distribution of desorption barriers, a phenomenon often observed in surface reactions that evinces intrinsic nonuniformities and demonstrates the inaptness of Langmuirian models.[54] The pronounced tail in the rate versus temperature profile indicates that CO_3* binding energies (and desorption barriers) increase as CO_2 desorbs and the "effective" extent of reduction increases. These inferences are consistent with CO_3* adsorbates that can preferentially stabilize O-atom removal transition states. Such effects are also responsible for the non-Langmuirian CO_3* coverage effects in CO oxidation reactions on $Ce_{0.5}Zr_{0.5}O_2$ (eqs 21 and 25). These nonidealities lead to catalytic rates that ultimately become insensitive to CO_2 at high CO_3* coverages, despite the competitive adsorption onto O* reactants, due to the compensating effect of intrinsic O* reactivities that increase with CO_3* coverage (Figure 8c).

The consequences of these thermodynamic nonidealities on CO_3* desorption rates preclude not only an unambiguous quantitative assessment of CO_2 binding strengths on $Ce_{0.5}Zr_{0.5}O_2$ ($\xi_{red,0}$ = 0) but also accurate comparisons with those on prereduced samples ($\xi_{red,0}$ > 0). Yet, a cursory assessment of their respective features during temperature ramping provides evidence for the expected relative coverages of CO_3* (at O*; the β term) and CO_2* (at *; the ω term) in eq 12. These data are shown in Figure 9 for $Ce_{0.5}Zr_{0.5}O_{1.91}$ ($\xi_{red,0}$ = 0.38; dark-gray) and $Ce_{0.5}Zr_{0.5}O_{1.83}$ ($\xi_{red,0}$ = 0.67; light-gray) and compared with the data for $Ce_{0.5}Zr_{0.5}O_2$ (black).

The onset of CO_2 evolution ($T_{onset}^{CO_2}$) from $Ce_{0.5}Zr_{0.5}O_{1.91}$ ($\xi_{red,0}$ = 0.38; dark-gray) occurs at 350 K, as in the case of $Ce_{0.5}Zr_{0.5}O_2$ (black), but rates reach a maximum ($T_{max}^{CO_2}$) at higher temperatures than on $Ce_{0.5}Zr_{0.5}O_2$ (540 K vs 430 K) and sustain detectable levels at temperatures above that at which CO_2 evolution from $Ce_{0.5}Zr_{0.5}O_2$ ceases (750 K). The total amount of CO_2 evolved (N_{CO_2}) is about 2-fold greater on $Ce_{0.5}Zr_{0.5}O_{1.91}$ (0.069 vs 0.032 mol mol_O^{-1}). The higher values of $T_{max}^{CO_2}$ and N_{CO_2} imply that the average CO_2 binding energy is higher on prereduced versus stoichiometric CZO crystals. Also, the rate versus temperature profile for $Ce_{0.5}Zr_{0.5}O_{1.91}$ exhibits, however subtle, an inflection point at 470 K, which occurs between the $T_{max}^{CO_2}$ values for $Ce_{0.5}Zr_{0.5}O_2$ (430 K) and $Ce_{0.5}Zr_{0.5}O_{1.91}$ (540 K). The coincidence in the $T_{onset}^{CO_2}$ values and the location of the inflection point together suggest that the broader peak for the prereduced sample comprises two peaks, each with a distinct distribution of binding strengths. One corresponds to the same CO_3* species formed on $Ce_{0.5}Zr_{0.5}O_2$ and the other to a CO_2-derived adsorbate with a higher mean binding strength, which can be tentatively assigned to a carboxylate-type species formed at anion vacancies (CO_2*).

On $Ce_{0.5}Zr_{0.5}O_{1.91}$ ($\xi_{red,0}$ = 0.38), but not on $Ce_{0.5}Zr_{0.5}O_2$, CO is detected during temperature ramping, with onset and maximum rates at 590 and 740 K (Figure 9, dashed dark-gray curve); these temperatures are higher than those required for the evolution of CO_2 from $Ce_{0.5}Zr_{0.5}O_{1.91}$ (350 and 540 K, respectively). Neither CO nor CO_2 were detected when $Ce_{0.5}Zr_{0.5}O_{2-x}$ ($\xi_{red,0} \geq 0$) was exposed to CO (2.0 kPa), instead of CO_2 (2.0 kPa), at 340 K, indicating that CO binds weakly to O-anions and anion vacancies, consistent with the first-order CO dependence in the stoichiometric (Figure 4a) and catalytic (Figure 8b) reactions. Thus, the CO that evolved upon heating CO_2-exposed $Ce_{0.5}Zr_{0.5}O_{1.91}$ crystals must have been formed from CO_2 bound at reduced centers (CO_2*) with the concomitant formation of O-anions; this is consistent with the reoxidation of CeO_{2-x} by CO_2[55,56] and with Ce-based

https://doi.org/10.1021/acscatal.4c04771
ACS Catal. 2024, 14, 16184−16204

Scheme 3. Transient Reaction-Convection System for Stoichiometric $Ce_{0.5}Zr_{0.5}O_2$ Reduction by CO

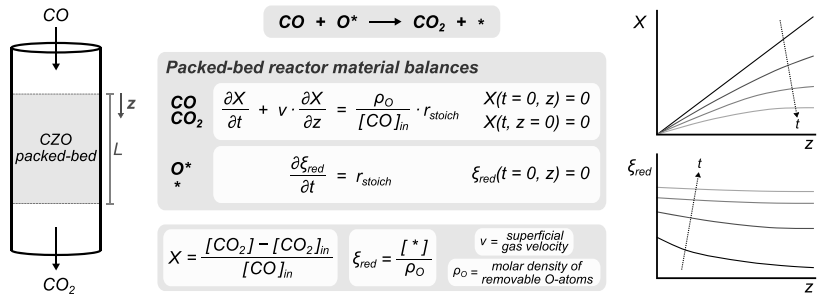

oxides acting as competent (but poor) catalysts for the (reverse) water–gas shift reaction.[57] These results show that surface carboxylates (CO_2*) undergo either desorption (CO_2* → CO_2 + *) or decomposition to reoxidize the reduced center (CO_2* → CO + O*), with relative rates that depend on temperature, coverage, and extent of reduction (*vide infra*).

The values of $T_{onset}^{CO_2}$ (350 K) and $T_{max}^{CO_2}$ (540 K) and the location of the inflection point (470 K) are similar for $Ce_{0.5}Zr_{0.5}O_{1.91}$ ($\xi_{red,0}$ = 0.38; solid dark-gray curve in Figure 9) and $Ce_{0.5}Zr_{0.5}O_{1.83}$ ($\xi_{red,0}$ = 0.67; solid light-gray curve), indicating that the same CO_3* and CO_2* adsorbates form upon exposing CZO to CO_2 irrespective of $\xi_{red,0}$. The amount of CO formed increases (0.080 versus 0.021 mol mol_O^{-1}) and the onset of its formation (450 K vs 590 K) and the maximum in rate (640 K vs 740 K) occur at lower temperatures as the extent of reduction increases ($\xi_{red,0}$ = 0.67 vs 0.38). These trends reflect thermodynamic limitations for CZO oxidation that lessen with increasing $\xi_{red,0}$, which matches expectations based on the reverse reaction; CZO reduction becomes more thermodynamically favorable as $\xi_{red,0}$ values decrease (Figure 2). The combined amounts of CO_2 and CO formed (0.032, 0.090, and 0.13 mol mol_O^{-1}) and the ratio of CO to CO_2 (0, 0.30, and 1.6) all increase monotonically with increasing $\xi_{red,0}$ (0, 0.38, and 0.67). These trends show that CO_2 binds more strongly at vacancies than O-anions. Consequently, the rate equations and mechanistic descriptions for stoichiometric CZO reduction by CO must include terms for CO_2* coverages and elementary steps for the adsorption of CO_2 at reduced centers, in contrast to the rate equation for CO oxidation catalysis (eq 21), which proceeds on CZO crystals with a dearth of vacancies.

3.5. Kinetics and Mechanism of Stoichiometric $Ce_{0.5}Zr_{0.5}O_2$ Reduction by CO. The combined evidence from

(i) redox thermodynamics (Section 3.1);

(ii) effects of CO and CO_2 on rate dependencies and assessments of reaction reversibility (Section 3.2);

(iii) solution-phase analogies and linear scaling relations (eqs 7 and 17–19);

(iv) mechanistic interpretations of rates of CO oxidation catalysis (Section 3.3);

(v) the comparison of CO_x evolution rates from fully oxidized and partially reduced CZO crystals with preadsorbed CO_2 (Section 3.4)

show that the elementary steps in Scheme 1 and a modified version of the rate equation proposed in Section 3.2 ($\hat{r}_{stoich}$, eq 12) can be used to describe the dynamics of stoichiometric reduction of CZO by CO:

$$r_{stoich} = \frac{[\alpha_{\ominus}\exp(m_{\alpha}\cdot\xi_{red})(1 + \lambda P_{CO_2})]P_{CO}}{1 + [\beta_{\ominus}\exp(m_{\beta}\cdot\xi_{red})]P_{CO_2} + [\omega_{\ominus}\exp(m_{\omega}\cdot\xi_{red})]\frac{\xi_{red}}{1-\xi_{red}}P_{CO_2}} \quad (26)$$

The three terms in the denominator of eq 26 (from left to right) reflect the relative coverages of O*, CO_3*, and CO_2*, where $\beta_{\ominus}$ and $\omega_{\ominus}$ represent the equilibrium constants for CO_2 binding onto O* and * (Steps β and ω in Scheme 1) for the ideal solution ($Ce_{0.5}Zr_{0.5}O_{2-x}$ with $\xi_{red} \to 0$); the exponentials with the m_{β} and m_{ω} parameters account for all thermodynamic nonidealities (eqs 18 and 19). The term within the square brackets in the numerator reflects the relative solubilities of the TS for CO-mediated O-atom removal and of O* reactants within the $Ce_{0.5}Zr_{0.5}O_{2-x}$ solution. The rate constant $\alpha_{\ominus}$ and the exponential with the m_{α} parameter (eq 17) represent the ideal solution ($\xi_{red} \to 0$) and excess Gibbs free energies of formation for the kinetically relevant transition state, respectively, and the $(1 + \lambda P_{CO_2})$ term captures how the presence of CO_3* adsorbates preferentially stabilize the O-atom removal TS (eq 25). Estimates for $\alpha_{\ominus}$, $\beta_{\ominus}$, and λ (eqs 22–24) were determined by regressing catalytic CO oxidation rate data (Figure 8) to the functional form of r_{cat} (eq 21).

Scheme 3 depicts the flow packed-bed system used in stoichiometric reduction reactions. The reaction-convection mole balance for gaseous molecules (CO and CO_2) is expressed in terms of the fractional CO_2 yield ($X = \Delta[CO_2]/[CO]_{in} = -\Delta[CO]/[CO]_{in}$), which varies with time (t) and axial position (z). The species within $Ce_{0.5}Zr_{0.5}O_{2-x}$ crystals (O* and *) do not convect along the bed, such that the mole balance, expressed in terms of ξ_{red} ($\propto[*] \propto (1 - [O^*])$), only involves the partial time derivative. Extents of reduction change along the packed-bed in response to changes in CO and CO_2 pressures via r_{stoich} (eq 26). Gas diffusion is fast, so that spatial gradients in the concentration of gaseous species within porous CZO aggregates (10^{-4} m) are kinetically inconsequential (Section S1; SI); no spatial gradients in O* and * chemical potentials within each CZO crystal (10^{-8} m) in such porous aggregates are present, because the "CZO solution" is "well-mixed" (*vide supra*, Section 3.1).[27]

The independent variables of the mole balances (t and z) are normalized by characteristic time and length scales (*vide infra*) so that the temporal and spatial derivatives of X and ξ_{red} become of order unity when the two coupled partial differential equations are expressed in dimensionless form:

$$\frac{\partial X}{\partial \bar{t}} = -\frac{1}{Da}\frac{\partial X}{\partial \bar{z}} + \bar{r}_{stoich} \qquad \begin{matrix} X(\bar{t} = 0, \bar{z}) = 0 \\ X(\bar{t}, \bar{z} = 0) = 0 \end{matrix} \quad (27)$$

https://doi.org/10.1021/acscatal.4c04771
ACS Catal. 2024, 14, 16184–16204

$$\frac{\partial \xi_{red}}{\partial \overline{t}} = \left(\frac{P_{CO,0}}{\rho_O RT}\right)\overline{r}_{stoich} \qquad \xi_{red}(\overline{t}=0,\overline{z})=0 \tag{28}$$

where $\overline{t}$ and $\overline{z}$ are dimensionless time and axial position, respectively, Da is the Damköhler number, R is the gas constant, ρ_O is the molar density of removable O-atoms within the packed-bed, and $\overline{r}_{stoich}$ is the dimensionless form of r_{stoich} (eq 26):

$$\overline{r}_{stoich} = \frac{\exp(m_\alpha \cdot \xi_{red})(1+\lambda P_{CO,0}(\Theta_{CO_2}+X))(1-X)}{1+\left(\beta_\ominus \exp(m_\beta \cdot \xi_{red}) + \omega_\ominus \exp(m_\omega \cdot \xi_{red})\frac{\xi_{red}}{1-\xi_{red}}\right)P_{CO,0}(\Theta_{CO_2}+X)} \tag{29}$$

Here, $P_{CO,0}$ is the CO pressure at the reactor inlet ($\overline{z}=0$) and Θ_{CO_2} is the ratio of CO_2 to CO pressures in the inlet reactant mixture. Axial position (z) is normalized to the packed-bed length ($\overline{z}=z/L$) and t to a time constant for the reaction (τ_{rxn}) defined as

$$\tau_{rxn} = (\alpha_\ominus \rho_O RT)^{-1} \tag{30}$$

The Damköhler number ($Da = \tau_{conv}/\tau_{rxn}$) is a ratio of convection ($\tau_{conv} = L/v$, where v is the superficial gas velocity) and reaction time constants and is calculated to be much smaller than unity at the examined conditions ($Da < 10^{-2}$). Thus, perturbation methods can be used to expedite numerical integration routines used to solve the system of nonlinear partial differential equations (eqs 27−29).[58]

The procedure for solving eqs 27−29 is described in Section S4 (SI) and briefly summarized here. The Damköhler number (Da) being much smaller than unity implies that spatial gradients evolve over time scales much longer than bed residence times (τ_{conv}). Thus, in a short time step ($\delta t \lesssim \tau_{conv}$), the magnitude of the time derivative on the left-hand side of eq 27 is much smaller than those for the terms on right-hand side, leading to an approximate "steady-state" reaction-convection equation for the gaseous species ($\partial X/\partial \overline{t} \approx 0$), which can be numerically solved by discretizing the axial domain into small finite elements. The resulting axial profile for X can then be used to solve the initial value problem for ξ_{red} (eq 28) at each finite element. Starting from the initial condition, cycles of spatial and temporal integrations of eq 27 and 28 are repeated until reaching the $\overline{t}$ value that corresponds to the end of the experiment.

Rate data for stoichiometric $Ce_{0.5}Zr_{0.5}O_2$ reduction at 648 K and a range of $P_{CO,0}$ (0.25−4.1 kPa CO) and Θ_{CO_2} (0.011−0.20) values were regressed to this transient reaction-convection model (eqs 27−29). The values of $\alpha_\ominus$, $\beta_\ominus$, and λ were kept at the values determined independently from CO catalytic oxidation rates (eqs 22−24); this decreased the number of free parameters from seven to four. Section S4 of the SI provides additional details about the regression methods. The regressed values of $\omega_\ominus$, m_α, m_β, and m_ω and their uncertainties (95% confidence intervals) are

$$\omega_\ominus = (0.075 \pm 0.011)\ \text{kPa}^{-1} \tag{31}$$

$$m_\alpha = -(7.6 \pm 0.72) \tag{32}$$

$$m_\beta = (0.64 \pm 0.23) \tag{33}$$

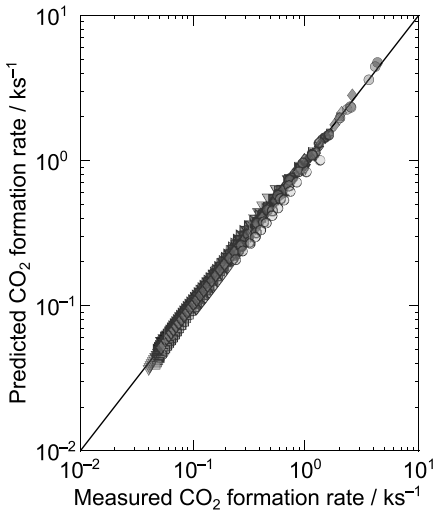

Figure 10. Comparison of predicted and measured CO_2 formation rates for stoichiometric $Ce_{0.5}Zr_{0.5}O_2$ reduction by CO at 648 K. The predictions were made using the transient reaction-convection model (eqs 27−29) and regressed parameter values in eqs 22−24 and 31−34. The symbol shapes denote reactions conducted with 0.25 (right-pointing triangles), 0.50 (down-pointing triangles), 1.0 (squares), 2.1 (diamonds), and 4.1 (circles) kPa CO in the reactant stream and the shading from dark-to-light denote increasing CO_2 pressures from 0.045−0.80 kPa.

$$m_\omega = (25 \pm 1.4) \tag{34}$$

Figure 10 shows a comparison of predicted and measured CO_2 formation (and O-atom removal) rates for 15 different conditions ($P_{CO,0}$ = 0.25−4.1 kPa CO and Θ_{CO_2} = 0.011−0.20); Figure 11 compares predicted and measured CO_2 rates as a function of time (and extent of reduction) for some of these conditions (the rest are shown in Section S4; SI). The small uncertainties (eqs 31−34) and the agreement between measured and predicted rates for the 900 measurements using parameter estimates in eqs 22−24 and 31−34 and the reaction-convection model given by eqs 27−29 show that these equations and mechanistic underpinnings accurately describe the removal of O-atoms from CZO crystals by CO. The effects of CO and CO_2 on r_{stoich} (eq 26) are well-described by the sequence of elementary steps in Scheme 1, and the consequences of thermodynamic nonidealities in the reduction−oxidation equilibria (eq 7) on the kinetic and thermodynamic parameters for these elementary steps (α, β, and ω) are accurately captured by the linear scaling relations represented by eqs 17−19.

These formalisms, both in their chemical and physical contexts, inform about how and why O-atom removal ceases before achieving reduction−oxidation equilibrium (Figure 5). Figure 12a shows model predictions for bed-averaged (*vide infra*; eq 35) O*, CO_3*, and CO_2* coverages ($\langle\theta_j\rangle$; for 4.1 kPa CO, 0.099 kPa CO_2). The bed-averaged coverage of carbonates, for example, is given by

https://doi.org/10.1021/acscatal.4c04771
ACS Catal. 2024, 14, 16184−16204

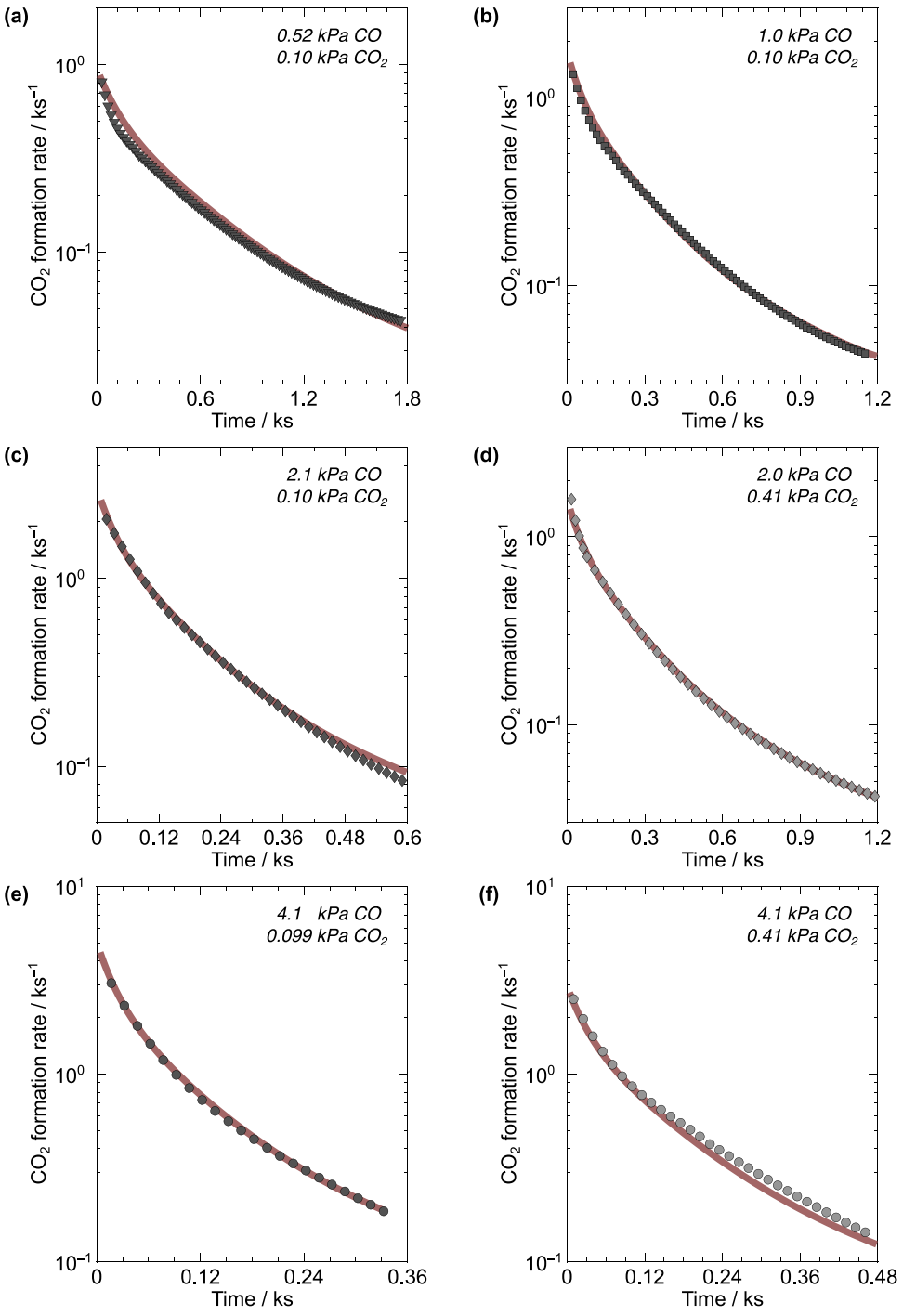

Figure 11. CO_2 formation rates versus time for reactions of CO and CO_2 mixtures with $Ce_{0.5}Zr_{0.5}O_2$ at 648 K. The symbols denote measured values and the solid curves predicted trends using the transient packed-bed reactor model (eqs 27−29) and the best-fit parameters listed in eqs 22−24 and 31−34.

$$\langle \theta_{CO_3*} \rangle = \int_0^1 \frac{\beta_\ominus \exp(m_\beta \cdot \xi_{red}) P_{CO,0}(\Theta_{CO_2} + X)}{1 + \left(\beta_\ominus \exp(m_\beta \cdot \xi_{red}) + \omega_\ominus \exp(m_\omega \cdot \xi_{red}) \frac{\xi_{red}}{1 - \xi_{red}}\right) P_{CO,0}(\Theta_{CO_2} + X)} d\bar{z} \quad (35)$$

Figure 12b shows the predicted ξ_{red} effects on γ_{O*}/γ_χ ratios (χ = CO_3*, TS, and CO_2*), which reflect the stabilities ("solubilities") of these various adsorbates ("solutes") relative to O* reactants as CZO crystals become reduced. In the early stages of CZO reduction ($\xi_{red} \ll 1$), CO_2* coverages are small and $Ce_{0.5}Zr_{0.5}O_{2-x}$ solutions contain CO_3* (dashed curve; Figure 12a) and O* (solid) solutes. As the reaction proceeds, rate-inhibiting CO_2* species become increasingly "soluble"

https://doi.org/10.1021/acscatal.4c04771
ACS Catal. 2024, 14, 16184−16204

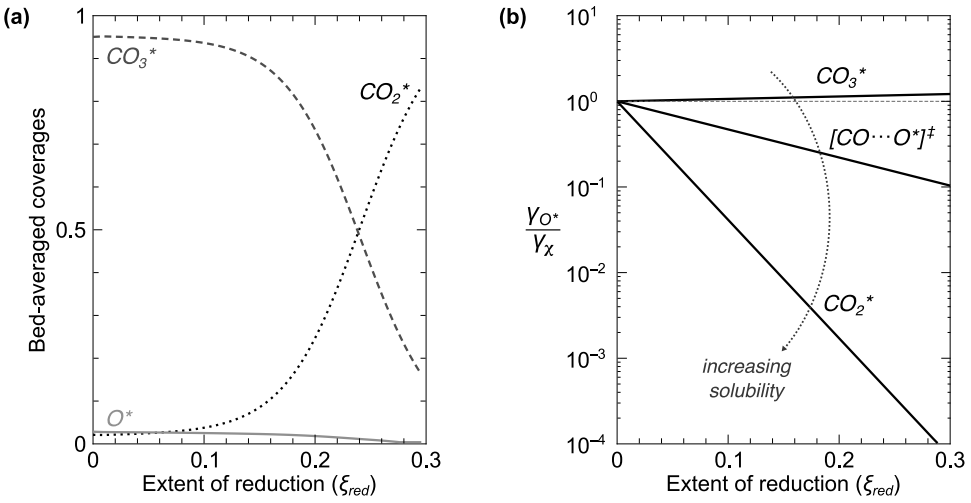

Figure 12. (a) Model predictions for bed-averaged coverages (eq 35) of oxygen anions (O*, solid light-gray), oxygen-bound carbonates (CO_3*, dashed dark-gray), and vacancy-bound carboxylates (CO_2*, dotted black) for $Ce_{0.5}Zr_{0.5}O_2$ reduction at 648 K with reactant stream comprising 4.1 kPa CO and 0.099 kPa CO_2. (b) Ranking the "solubility" of kinetically relevant "solutes" within $Ce_{0.5}Zr_{0.5}O_{2-x}$ "solutions" during CZO reduction by CO at 648 K. The abscissa values are extents of CZO reduction ($\xi_{red} = 4x$).

compared to both CO_3* and O-atom removal transition states ($[CO\cdots O^*]^{\ddagger}$; Figure 12b). Thus, CO_2* adsorbates eventually cover most of the surface redox sites (dotted curve; Figure 12a) and kinetic hurdles for O-atom removal reflect the combination of barriers for exsolving highly soluble CO_2* species from the CZO solution and dissolving significantly less-soluble $[CO\cdots O^*]^{\ddagger}$ transition states. This disparity in solubility increases with reaction progress, thus leading to O-atom removal rates that reach undetectable levels at ξ_{red} values that are well below those that correspond to redox equilibrium.

This effect of changes to the relative solubilities of TS and CO_2* solutes with ξ_{red} on CZO rates are also evident in the k_{app} versus ξ_{red} curves (Figure 4). The initial slopes of k_{app} with respect to ξ_{red} (on a semilogarithmic scale; $\partial \ln k_{app}/\partial \xi_{red}$) at early stages ($\xi_{red} < 0.2$) reflect the linear scaling relation between the free energy of formation of $[CO\cdots O^*]^{\ddagger}$ ($\Delta G_{\alpha}^{\ddagger}$; eq 13) and the equilibrium reduction free energy (ΔG_{red}; eq 6). The coverage and solubility of CO_2* increase as the solutions become depleted of O* and enriched in *, leading to $\partial \ln k_{app}/\partial \xi_{red}$ values that reflect the scaling relation between the free energy of formation of CO_2* and ΔG_{red}.

The model predictions (Figure 12) provide insights about design strategies for using Ce-based materials as O-storage media in emissions control and chemical looping. The binding strength of CO_2* should be assessed when evaluating candidate oxygen storage materials, since these spectators inhibit reduction rates and thus prevent the buffer/carrier from utilizing its entire oxygen storage capacity, a thermodynamic metric often measured and/or calculated when evaluating candidates.[19,21−23] This kinetic inhibition is also likely to be prevalent during catalytic CO oxidation, hydrocarbon and soot combustion, and (reverse) water−gas shift reactions, all of which occur in emissions control practice on catalysts that comprise metal nanoparticles dispersed on Ce-based oxides. These reactions proceed through mechanisms in which oxidants (O_2, CO_2, or H_2O) are activated at reduced centers on the oxide surface to form O-atoms that then diffuse to metal clusters where they are consumed by reductants (CO, C, or H_2).[57,59−61] The formation of strongly bound CO_2 adsorbates on reduced centers inhibit oxide-to-metal O-atom fluxes and thus turnover frequencies.

3.6. Implications and Treatments of Thermodynamic Non-Idealities and Chemical Dynamics in Adjacent Chemistries.

The nonequilibrium thermodynamic constructs used here to discern the mechanism of the surface reactions that determine CZO reduction rates are relevant in general to stoichiometric chemical reactions. Such general applicability reflects their reliance on chemical potentials as the relevant driving forces, whether for physical or chemical processes, because they represent the dynamics at which such processes approach equilibrium.

CZO reduction rates depend on free energy differences between the O-atom removal transition state and its O* reactant precursors, while CZO oxidation rates reflect O* (and *) lattice diffusion, which is driven by intracrystal spatial gradients in O* chemical potentials ($j_{O^*} \propto \nabla \mu_{O^*}$).[27] The transport dynamics in O-atom addition to CZO can be accurately captured using free energy relations and diffusion-convection constructs that are similar to those used for surface reaction rates in O-atom removal.[62] Free energy differences and O* chemical potential gradients also drive the reduction and oxidation rates of other metal oxides, rendering the concepts used here adaptable to describe, for instance, redox cycling of Fe-based oxides and perovskites used in chemical looping processes[19,61] and ion transport fluxes within oxygen and proton conducting electrolytes used in fuel cells.[63,64]

The (thermo)dynamics of CO_2 capture using amine-based sorbents are driven by differences between the CO_2 chemical potential in the sorbent and gaseous states. The form of equilibrium sorption isotherms on sterically hindered amines[65,66] and grafted diamine moieties in metal−organic frameworks[67,68] do not obey Langmuirian (ideal) formalisms, but instead reflect CO_2 binding energies that are highly sensitive to coverage. The use of the solution-phase (nonideal) thermodynamics lexicon proposed here together with free energy relations between measured isosteric adsorption free energies and (excess) free energies of formation for CO_2 binding transition states (analogous to that between ΔG_{red}^{E} and $\Delta G_{\alpha}^{E,\ddagger}$; eqs 7, 13, and 17) may lead to kinetic models for CO_2 adsorption and desorption that can leverage the extensive CO_2 sorption thermodynamic archival data.[65−70] Such approaches can provide mechanistic insights that guide the

https://doi.org/10.1021/acscatal.4c04771
ACS Catal. 2024, 14, 16184−16204

search for sorbent design criteria that encompass thermodynamic metrics, such as uptake capacities, as well as rate and equilibrium constants that determine intrinsic rates of uptake and release.

(De)lithiation rates of carbon-based anodes and layered oxide cathodes used in Li-ion batteries are driven by Li^+ (electro)chemical potential gradients. Physics-based reaction-transport models that have been developed to accurately describe these dynamics use Butler−Volmer equations, which depict electrochemical kinetic driving forces as overpotentials ($\eta = \phi - \phi_{oc}$), and rely on measurements of how open circuit potentials of working electrodes (ϕ_{oc}) depend on extent of lithiation (ξ_{Li}).[1,71−73] The CZO reduction−oxidation thermodynamic measurements that inform about the functional dependence of ΔG^E_{red} on ξ_{red} (Figure 2 and eq 7) are similar in concept to those used to elaborate how ϕ_{oc} depends on ξ_{Li}. Electrochemical kinetic equations can therefore be rigorously formulated using transition state formalisms as the starting point.[2,74,75] The nonequilibrium thermodynamics basis of transition state theory guides in a more direct manner, and without reference to phenomenological charge transfer coefficients, the identification of scaling relations between equilibrium and kinetic driving forces (e.g., eqs 17−19) and their use in models for the dynamics of (dis)charge during stoichiometric electrode (de)lithiation. The use of nonideal solution-phase thermodynamic conventions may also help to discern the modes of degradation of $LiMO_2$ cathodes, which can occur via O_2 evolution and undesired side reactions with the contacting electrolyte.[76]

The use of transition state theory and free energy scaling relations to model and predict reaction dynamics, to corroborate mechanistic proposals, and to identify materials and process design criteria can be applied to many other systems across all areas of chemistry, since these constructs are founded upon universal laws of mass action and thermodynamics. This generalizable approach provides a framework to communicate the lessons learned from investigating, for instance, CZO reduction−oxidation cycles relevant to emissions control practice using the widely spoken lexicon of thermodynamics—an effort to facilitate dialog among researchers and practitioners in (seemingly) disparate fields.

4. CONCLUSIONS

Chemical kinetics represent an essential tool to optimize reactions and investigate their mechanisms. In many systems, kinetic data can be accurately described by rate equations based on an "ideal" form of the law of mass action in which rates of elementary steps are proportional to reactant concentrations. Nonidealities prevail in stoichiometric reactions at fluid−solid interfaces, a class of systems that includes battery (dis)charge, wastewater treatment, and carbon sequestration. The use of kinetics to develop molecular-level understanding of these processes requires methods and formalisms to measure and analyze rates that are instead proportional to reactant activities. Such protocols are described and used here for $Ce_{0.5}Zr_{0.5}O_{2-x}$ (CZO) reduction, a system relevant to emissions control practice, chemical looping oxidations, and ion transport membranes.

The equilibrium free energy penalty incurred upon removing an O-atom from $Ce_{0.5}Zr_{0.5}O_{2-x}$ (ΔG_{red}) becomes increasingly costly as the extent of CZO reduction ($\xi_{red} = 4x$) increases. These nonidealities in the reduction−oxidation thermodynamics manifest in the dynamics of CZO reduction as kinetic free energy barriers for O-atom removal that depend on ξ_{red}. The consequences of thermodynamic nonidealities on reduction kinetics are interpreted and articulated here using concepts and vernacular of solution thermodynamics and transition state theory. These treatments lead to an accurate mechanistically derived kinetic model for CZO reduction by CO. The model employs an analogy to fluid-phase equilibria, in which lattice oxygen anions (O*), anion vacancies (*), surface-bound intermediates, and transition states are depicted as solutes that interact with the CZO solvent in a well-mixed solution. Bulk lattice diffusion is much faster than the surface reaction during CZO reduction by CO, rendering intracrystal O* and * chemical potentials uniform and CZO solutions well-mixed. The stoichiometric oxide ($\xi_{red} = 0$) is defined as the "ideal solution" such that nonidealities are represented by nonunity activity coefficients (and nonzero excess Gibbs free energies) for nonstoichiometric oxides ($\xi_{red} \neq 0$).

Measured ΔG_{red} values reflect the relative solubilities of O* and * solutes and can be described by a single-valued function of ξ_{red}. Free energy relations then imply that the solubilities of intermediates and transition states are also single-valued functions of ξ_{red}. CZO reduction rates, when compared at similar ξ_{red} values, are first-order in CO and inhibited by CO_2, showing that the kinetically relevant transition state involves a fleeting adduct between CO and O* and that CO_2 blocks surface redox sites. These kinetic trends for the stoichiometric reaction were corroborated by a kinetic study of CO oxidation catalysis, which also gives estimates of the rate and equilibrium constants that parametrize the stoichiometric reduction rate equation for the "ideal solution", since steady-state CO oxidation rates are zero-order in O_2. Turnover rates on $Ce_{0.5}Zr_{0.5}O_2$ are inhibited by CO_2, showing that CO_2 binds onto oxidized centers to form site-blocking carbonates. High carbonate coverages on stoichiometric surfaces lead to "overoxidized" crystals (i.e., apparent negative extents of reduction) that induce preferential stabilization of O-atom removal transition states, demonstrating that nonidealities emerge even for the ideal solution and evincing non-Langmuirian effects in oxidation catalysis on Ce-based oxides. Temperature-ramping experiments on (non)stoichiometric CZO crystals with preadsorbed CO_2 show that CO_2 also binds onto reduced centers to form carboxylates. These mechanistic insights lead to a rate equation that, when embedded into partial differential equations that describe reaction-convection phenomena in transient packed-bed reactors, predicts measured stoichiometric reduction rates with high fidelity.

The model shows that CZO reduction by CO, at conditions resembling those for "cold start" of emissions control systems, ceases well before the thermodynamically prescribed oxygen storage capacity is consumed because rate-inhibiting carboxylates become increasingly soluble relative to O-atom removal transition states as ξ_{red} increases. These insights suggest that the performance of Ce-based oxides as oxygen buffers and carriers in emissions control and chemical looping can be improved by modifying them to avoid the formation of strongly bound carboxylates. The protocols and formalisms described herein illustrate how the tenets of transition state theory and nonideal thermodynamics can be used so that chemical kinetics can inform on underlying mechanisms and materials design criteria for stoichiometric processes that embody strong thermodynamic nonidealities, which arise not

https://doi.org/10.1021/acscatal.4c04771
ACS Catal. 2024, 14, 16184−16204

only in emissions control practice but also in energy storage, environmental remediation, and CO_2 capture.

■ ASSOCIATED CONTENT

Supporting Information

The Supporting Information is available free of charge at https://pubs.acs.org/doi/10.1021/acscatal.4c04771.

Calculations verifying the absence of inter- and intra-phase mass transport artifacts; criterion for reduction–oxidation equilibrium; parameter estimation for catalytic CO oxidation on $Ce_{0.5}Zr_{0.5}O_2$; perturbation and numerical methods and parameter estimation for stoichiometric $Ce_{0.5}Zr_{0.5}O_2$ reduction by CO (PDF)

■ AUTHOR INFORMATION

Corresponding Author

Enrique Iglesia − *Department of Chemical and Biomolecular Engineering, University of California, Berkeley, Berkeley, California 94720, United States; Charles D. Davidson School of Chemical Engineering, Purdue University, West Lafayette, Indiana 47907, United States;* orcid.org/0000-0003-4109-1001; Email: iglesia@berkeley.edu

Authors

Andrew Hwang − *Department of Chemical and Biomolecular Engineering, University of California, Berkeley, Berkeley, California 94720, United States*

Andrew "Bean" Getsoian − *Research and Advanced Engineering, Ford Motor Company, Dearborn, Michigan 48124, United States;* orcid.org/0000-0003-1534-3818

Complete contact information is available at: https://pubs.acs.org/10.1021/acscatal.4c04771

Notes

Indemnification: While this article is believed to contain correct information, Ford Motor Company (Ford) does not expressly or impliedly warrant, nor assume any responsibility, for the accuracy, completeness, or usefulness of any information, apparatus, product, or process disclosed, nor represent that its use would not infringe the rights of third parties. Reference to any commercial product or process does not constitute its endorsement. This article does not provide financial, safety, medical, consumer product, or public policy advice or recommendation. Readers should independently replicate all experiments, calculations, and results. The views and opinions expressed are of the authors and do not necessarily reflect those of Ford. This disclaimer may not be removed, altered, superseded, or modified without prior Ford permission.

The authors declare no competing financial interest.

■ ACKNOWLEDGMENTS

This study was financially supported by the Ford Motor Company and the Vermeulen Chair endowment fund.

■ REFERENCES

(1) Karthikeyan, D. K.; Sikha, G.; White, R. E. Thermodynamic Model Development for Lithium Intercalation Electrodes. *J. Power Sources* **2008**, *185*, 1398−1407.

(2) Bazant, M. Z. Theory of Chemical Kinetics and Charge Transfer Based on Nonequilibrium Thermodynamics. *Acc. Chem. Res.* **2013**, *46*, 1144−1160.

(3) Eyring, H. The Activated Complex in Chemical Reactions. *J. Chem. Phys.* **1935**, *3*, 107−115.

(4) Wynne-Jones, W. F. K.; Eyring, H. The Absolute Rate of Reactions in Condensed Phases. *J. Chem. Phys.* **1935**, *3*, 492−502.

(5) Evans, M. G.; Polanyi, M. Some Applications of the Transition State Method to the Calculation of Reaction Velocities, Especially in Solution. *Trans. Faraday Soc.* **1935**, *31*, 875−894.

(6) Horiuti, J. On the Statistical Mechanical Treatment of the Absolute Rate of Chemical Reaction. *Bull. Chem. Soc. Jpn.* **1938**, *13*, 210−216.

(7) Laidler, K. J. Elementary Reactions in Solution. In *Chemical Kinetics*, 3rd ed.; Harper & Row, 1987; pp 183−228.

(8) Espenson, J. H. Reactions in Solution. In *Chemical Kinetics and Reaction Mechanisms*; McGraw-Hill, 1981; pp 166−181.

(9) Reichardt, C.; Welton, T. Solvent Effects on the Rates of Homogeneous Chemical Reactions. In *Solvents and Solvent Effects in Organic Chemistry*, 4th ed.; Wiley-VCH, 2011; pp 165−357.

(10) Bard, A. J.; Faulkner, L. R. Kinetics of Electrode Reactions. In *Electrochemical Methods: Fundamentals and Applications*, 2nd ed.; John Wiley & Sons, 2001; pp 87−136.

(11) Boudart, M.; Djéga-Mariadassou, G. Structure-Insensitive and Structure-Sensitive Reactions on Metals. In *Kinetics of Heterogeneous Catalytic Reactions*; Princeton University Press, 1984; pp 155−193.

(12) Madon, R. J.; Iglesia, E. Catalytic Reaction Rates in Thermodynamically Non-Ideal Systems. *J. Mol. Catal. A: Chem.* **2000**, *163*, 189−204.

(13) Bhan, A.; Iglesia, E. A Link Between Reactivity and Local Structure in Acid Catalysis on Zeolites. *Acc. Chem. Res.* **2008**, *41*, 559−567.

(14) Gounder, R.; Iglesia, E. The Catalytic Diversity of Zeolites: Confinement and Solvation Effects within Voids of Molecular Dimensions. *Chem. Commun.* **2013**, *49*, 3491−3509.

(15) Sarazen, M. L.; Iglesia, E. Effects of Charge, Size, and Shape of Transition States, Bound Intermediates, and Confining Voids in Reactions of Alkenes on Solid Acids. *ChemCatChem* **2018**, *10*, 4028−4037.

(16) Agirrezabal-Telleria, I.; Iglesia, E. Mechanistic Insights and Consequences of Intrapore Liquids in Ethene, Propene, and Butene Dimerization on Isolated Ni^{2+} Sites Grafted within Aluminosilicate Mesopores. *J. Catal.* **2020**, *389*, 690−705.

(17) Bates, J. S.; Gounder, R. Kinetic Effects of Molecular Clustering and Solvation by Extended Networks in Zeolite Acid Catalysis. *Chem. Sci.* **2021**, *12*, 4699−4708.

(18) Potts, D. S.; Bregante, D. T.; Adams, J. S.; Torres, C.; Flaherty, D. W. Influence of Solvent Structure and Hydrogen Bonding on Catalysis at Solid−Liquid Interfaces. *Chem. Soc. Rev.* **2021**, *50*, 12308−12337.

(19) Luo, S.; Zeng, L.; Fan, L.-S. Chemical Looping Technology: Oxygen Carrier Characteristics. *Annu. Rev. Chem. Biomol. Eng.* **2015**, *6*, 53−75.

(20) Inaba, H.; Tagawa, H. Ceria-Based Solid Electrolytes. *Solid State Ionics* **1996**, *83*, 1−16.

(21) Jen, H.-W.; Graham, G. W.; Chun, W.; McCabe, R. W.; Cuif, J.-P.; Deutsch, S. E.; Touret, O. Characterization of Model Automotive Exhaust Catalysts: Pd on Ceria and Ceria−Zirconia Supports. *Catal. Today* **1999**, *50*, 309−328.

(22) Shelef, M.; McCabe, R. W. Twenty-Five Years After Introduction of Automotive Catalysts: What Next? *Catal. Today* **2000**, *62*, 35−50.

(23) Trovarelli, A.; de Leitenburg, C.; Boaro, M.; Dolcetti, G. The Utilization of Ceria in Industrial Catalysis. *Catal. Today* **1999**, *50*, 353−367.

(24) Mogensen, M.; Sammes, N. M.; Tompsett, G. A. Physical, Chemical and Electrochemical Properties of Pure and Doped Ceria. *Solid State Ionics* **2000**, *129*, 63−94.

(25) Zhou, G.; Shah, P. R.; Kim, T.; Fornasiero, P.; Gorte, R. J. Oxidation Entropies and Enthalpies of Ceria-Zirconia Solid Solutions. *Catal. Today* **2007**, *123*, 86−93.

(26) Kuhn, M.; Bishop, S. R.; Rupp, J. L. M.; Tuller, H. L. Structural Characterization and Oxygen Nonstoichiometry of Ceria-Zirconia ($Ce_{1-x}Zr_xO_{2-\delta}$) Solid Solutions. *Acta Mater.* **2013**, *61*, 4277−4288.
(27) Hwang, A.; Wu, J.; Getsoian, A.; Iglesia, E. Kinetic Relevance of Surface Reactions and Lattice Diffusion in the Dynamics of Ce-Zr Oxides Reduction-Oxidation Cycles. *J. Phys. Chem. C* **2023**, *127*, 2936−2952.
(28) Madon, R. J.; Boudart, M. Experimental Criterion for the Absence of Artifacts in the Measurement of Rates of Heterogeneous Catalytic Reactions. *Ind. Eng. Chem. Fundam.* **1982**, *21*, 438−447.
(29) Mizusaki, J.; Yamauchi, S.; Fueki, K.; Ishikawa, A. Nonstoichiometry of the Perovskite-Type Oxide $La_{1-x}Sr_xCrO_{3-\delta}$. *Solid State Ionics* **1984**, *12*, 119−124.
(30) Scheffe, J. R.; Steinfeld, A. Thermodynamic Analysis of Cerium-Based Oxides for Solar Thermochemical Fuel Production. *Energy Fuels* **2012**, *26*, 1928−1936.
(31) Hao, Y.; Yang, C.-K.; Haile, S. M. Ceria-Zirconia Solid Solutions ($Ce_{1-x}Zr_xO_{2-\delta}$, $x \leq 0.2$) for Solar Thermochemical Water Splitting: A Thermodynamic Study. *Chem. Mater.* **2014**, *26*, 6073−6082.
(32) Rink, J.; Meister, N.; Herbst, F.; Votsmeier, M. Oxygen Storage in Three-Way-Catalysts is an Equilibrium Controlled Process: Experimental Investigation of the Redox Thermodynamics. *Appl. Catal., B* **2017**, *206*, 104−114.
(33) Boudart, M. Virtual Pressure and Virtual Fugacity in Catalysis and Electrocatalysis. *Catal. Lett.* **1989**, *3*, 111−115.
(34) Chase, M. W., Jr. NIST-JANAF Thermochemical Tables, 4th Ed. *J. Phys. Chem. Ref. Data* **1998**, *25*, 1−1951.
(35) (a) Standard State. In *IUPAC Compendium of Chemical Terminology*, 3rd ed.; International Union of Pure and Applied Chemistry, 2006. Online version 3.0.1, 2019. (b) Activity. In *IUPAC Compendium of Chemical Terminology*, 3rd ed.; International Union of Pure and Applied Chemistry, 2006.
(36) Lewis, G. N.; Randall, M. The Useful Functions, Activity, Activity Coefficients, and Equilibrium Constant. In *Thermodynamics*, 2nd ed.; Pitzer, K. S.; Brewer, L., Eds.; McGraw-Hill, 1961; pp 242−279.
(37) Prausnitz, J. M.; Lichtenthaler, R. N.; Gomes de Azevedo, E. Fugacities in Liquid Mixtures: Excess Functions. In *Molecular Thermodynamics of Fluid-Phase Equilibria*, 3rd ed.; Prentice Hall, 1999; pp 213−305.
(38) Scrosati, B.; Vincent, C. A.; McKechnie, J. S.; Scrosati, B. Alkali Metal, Alkaline-Earth Metal, and Ammonium Halides. Amide Solvents. In *Solubility Data Series*, 1st ed.; International Union of Pure and Applied Chemistry; Pergamon Press, 1980; Vol. *11*, pp 162−167.
(39) Lewis, G. N.; Randall, M. Theories of Electrolyte Solutions. In *Thermodynamics*, 2nd ed.; revised by Pitzer, K. S.; Brewer, L., Eds.; McGraw-Hill, 1961; pp 332−348.
(40) Prausnitz, J. M.; Lichtenthaler, R. N.; Gomes de Azevedo, E. Electrolyte Solutions. In *Molecular Thermodynamics of Fluid-Phase Equilibria*, 3rd ed.; Prentice Hall, 1999; pp 507−581.
(41) Navrotsky, A.; Ma, C.; Lilova, K.; Birkner, N. Nanophase Transition Metal Oxides Show Large Thermodynamically Driven Shifts in Oxidation-Reduction Equilibria. *Science* **2010**, *330*, 199−201.
(42) Chen, G.; Thompson, A.; Gorski, C. A. Disentangling the Size-Dependent Redox Reactivity of Iron Oxides Using Thermodynamic Relationships. *Proc. Natl. Acad. Sci. U.S.A.* **2022**, *119*, No. e2204673119.
(43) Brus, L. E. Electron-Electron and Electron-Hole Interactions in Small Semiconductor Crystallites: The Size Dependence of the Lowest Excited Electronic State. *J. Chem. Phys.* **1984**, *80*, 4403−4409.
(44) Norris, D. J.; Bawendi, M. G. Measurement and Assignment of the Size-Dependent Optical Spectrum in CdSe Quantum Dots. *Phys. Rev. B* **1996**, *53*, 16338−16346.
(45) Mars, P.; van Krevelen, D. W. Oxidations Carried Out by Means of Vanadium Oxide Catalysts. *Chem. Eng. Sci.* **1954**, *3*, 41−59.
(46) Kwon, S.; Deshlahra, P.; Iglesia, E. Dioxygen Activation Routes in Mars-van Krevelen Redox Cycles Catalyzed by Metal Oxides. *J. Catal.* **2018**, *364*, 228−247.
(47) Madier, Y.; Descorme, C.; Le Govic, A. M.; Duprez, D. Oxygen Mobility in CeO_2 and $Ce_xZr_{(1-x)}O_2$ Compounds: Study by CO Transient Oxidation and $^{18}O/^{16}O$ Isotopic Exchange. *J. Phys. Chem. B* **1999**, *103*, 10999−11006.
(48) Getsoian, A. B.; Zhai, Z.; Bell, A. T. Band-Gap Energy as a Descriptor of Catalytic Activity for Propene Oxidation over Mixed Metal Oxide Catalysts. *J. Am. Chem. Soc.* **2014**, *136*, 13684−13697.
(49) Hattori, H. Heterogeneous Basic Catalysis. *Chem. Rev.* **1995**, *95*, 537−558.
(50) Zhang, Z.; Yates, J. T., Jr. Band Bending in Semiconductors: Chemical and Physical Consequences at Surfaces and Interfaces. *Chem. Rev.* **2012**, *112*, 5520−5551.
(51) Vayssilov, G. N.; Mihaylov, M.; St Petkov, P.; Hadjiivanov, K. I.; Neyman, K. M. Reassignment of the Vibrational Spectra of Carbonates, Formates, and Related Surface Species on Ceria: A Combined Density Functional and Infrared Spectroscopy Investigation. *J. Phys. Chem. C* **2011**, *115*, 23435−23454.
(52) Cheng, Z.; Sherman, B. J.; Lo, C. S. Carbon Dioxide Activation and Dissociation on Ceria (110): A Density Functional Theory Study. *J. Chem. Phys.* **2013**, *138*, No. 014702.
(53) Albrecht, P. M.; Jiang, D.; Mullins, D. R. CO_2 Adsorption as a Flat-Lying, Tridentate Carbonate on CeO_2(100). *J. Phys. Chem. C* **2014**, *118*, 9042−9050.
(54) Ho, T. C.; Aris, R. On Apparent Second-Order Kinetics. *AIChE J.* **1987**, *33*, 1050−1051.
(55) Sharma, S.; Hilaire, S.; Vohs, J. M.; Gorte, R. J.; Jen, H.-W. Evidence for Oxidation of Ceria by CO_2. *J. Catal.* **2000**, *190*, 199−204.
(56) Staudt, T.; Lykhach, Y.; Tsud, N.; Skála, T.; Prince, K. C.; Matolín, V.; Libuda, J. Ceria Reoxidation by CO_2: A Model Study. *J. Catal.* **2010**, *275*, 181−185.
(57) Gorte, R. J. Ceria in Catalysis: From Automotive Applications to the Water-Gas Shift Reaction. *AIChE J.* **2010**, *56*, 1126−1135.
(58) Deen, W. M. Scaling and Approximation Techniques. In *Analysis of Transport Phenomena*, 1st ed.; Oxford University Press, 1998; pp 73−131.
(59) Zafiris, G. S.; Gorte, R. J. Evidence for Low-Temperature Oxygen Migration from Ceria to Rh. *J. Catal.* **1993**, *139*, 561−567.
(60) Zafiris, G. S.; Gorte, R. J. Evidence for a Second CO Oxidation Mechanism on Rh/Ceria. *J. Catal.* **1993**, *143*, 86−91.
(61) Pei, C.; Chen, S.; Fu, D.; Zhao, Z.-J.; Gong, J. Structured Catalysts and Catalytic Processes: Transport and Reaction Perspectives. *Chem. Rev.* **2024**, *124*, 2955−3012.
(62) Hwang, A.; Wu, J.; Getsoian, A.; Iglesia, E., To be submitted.
(63) Lin, Y.-S.; Wang, W.; Han, J. Oxygen Permeation Through Thin Mixed-Conducting Solid Oxide Membranes. *AIChE J.* **1994**, *40*, 786−798.
(64) Eikerling, M.; Kornyshev, A. A.; Kuznetsov, A. M.; Ulstrup, J.; Walbran, S. Mechanisms of Proton Conductance in Polymer Electrolyte Membranes. *J. Phys. Chem. B* **2001**, *105*, 3646−3662.
(65) Sartori, G.; Savage, D. W. Sterically Hindered Amines for Carbon Dioxide Removal from Gases. *Ind. Eng. Chem. Fundam.* **1983**, *22*, 239−249.
(66) Versteeg, G. F.; van Dijck, L. A. J.; van Swaaij, W. P. M. On the Kinetics Between CO_2 and Alkanolamines Both in Aqueous and Non-Aqueous Solutions. An Overview. *Chem. Eng. Commun.* **1996**, *144*, 113−158.
(67) Martell, J. D.; Milner, P. J.; Siegelman, R. L.; Long, J. R. Kinetics of Cooperative CO_2 Adsorption in Diamine-Appended Variants of the Metal-Organic Framework Mg_2(dobpdc). *Chem. Sci.* **2020**, *11*, 6457−6471.
(68) Darunte, L. A.; Sen, T.; Bhawanani, C.; Walton, K. S.; Sholl, D. S.; Realff, M. J.; Jones, C. W. Moving Beyond Adsorption Capacity in Design of Adsorbents for CO_2 Capture from Ultradilute Feeds: Kinetics of CO_2 Adsorption in Materials with Stepped Isotherms. *Ind. Eng. Chem. Res.* **2019**, *58*, 366−377.

https://doi.org/10.1021/acscatal.4c04771
ACS Catal. 2024, 14, 16184−16204

(69) Puxty, G.; Rowland, R.; Allport, A.; Yang, Q.; Bown, M.; Burns, R.; Maeder, M.; Attalla, M. Carbon Dioxide Postcombustion Capture: A Novel Screening Study of the Carbon Dioxide Absorption Performance of 76 Amines. *Environ. Sci. Technol.* **2009**, *43*, 6427−6433.
(70) Zheng, C.; Yang, X.; Li, M.; Bai, S. Bridging the Adsorption Data and Adsorption Process by Introducing a Polynomial Structure to Accurately Describe IUPAC Isotherms, Stepwise Isotherms, and Stepwise Breakthrough Curves. *Langmuir* **2024**, *40*, 4132−4141.
(71) Doyle, M.; Fuller, T. F.; Newman, J. Modeling of Galvanostatic Charge and Discharge of the Lithium/Polymer/Insertion Cell. *J. Electrochem. Soc.* **1993**, *140*, 1526−1533.
(72) Levi, M. D.; Aurbach, D. Frumkin Intercalation Isotherm — A Tool for the Description of Lithium Insertion Into Host Materials: A Review. *Electrochim. Acta* **1999**, *45*, 167−185.
(73) Sethuraman, V. A.; Srinivasan, V.; Newman, J. Analysis of Electrochemical Lithiation and Delithiation Kinetics in Silicon. *J. Electrochem. Soc.* **2013**, *160*, A394−A403.
(74) Ferguson, T. R.; Bazant, M. Z. Nonequilibrium Thermodynamics of Porous Electrodes. *J. Electrochem. Soc.* **2012**, *159*, A1967−A1985.
(75) Dickinson, E. J. F.; Wain, A. J. The Butler-Volmer Equation in Electrochemical Theory: Origins, Value, and Practical Application. *J. Electroanal. Chem.* **2020**, *872*, No. 114145.
(76) Dose, W. M.; Li, W.; Temprano, I.; O'Keefe, C. A.; Mehdi, B. L.; De Volder, M. F. L.; Grey, C. P. Onset Potential for Electrolyte Oxidation and Ni-Rich Cathode Degradation in Lithium-Ion Batteries. *ACS Energy Lett.* **2022**, *7*, 3524−3530.

https://doi.org/10.1021/acscatal.4c04771
ACS Catal. 2024, 14, 16184−16204